Multiciliated cell basal bodies align in stereotypical patterns coordinated by the apical cytoskeleton

Elisa Herawati,[1]* Daisuke Taniguchi,[2]* Hatsuho Kanoh,[1,3] Kazuhiro Tateishi,[1] Shuji Ishihara,[2] and Sachiko Tsukita[1]

[1]Laboratory of Biological Science, Graduate School of Frontier Biosciences and Graduate School of Medicine, Osaka University, Osaka 565-0871, Japan
[2]Department of Physics, School of Science and Technology, Meiji University, Kanagawa 214-8571, Japan
[3]Faculty of Science, Kyoto University, Kyoto 606-8502, Japan

Multiciliated cells (MCCs) promote fluid flow through coordinated ciliary beating, which requires properly organized basal bodies (BBs). Airway MCCs have large numbers of BBs, which are uniformly oriented and, as we show here, align linearly. The mechanism for BB alignment is unexplored. To study this mechanism, we developed a long-term and high-resolution live-imaging system and used it to observe green fluorescent protein–centrin2–labeled BBs in cultured mouse tracheal MCCs. During MCC differentiation, the BB array adopted four stereotypical patterns, from a clustering "floret" pattern to the linear "alignment." This alignment process was correlated with BB orientations, revealed by double immunostaining for BBs and their asymmetrically associated basal feet (BF). The BB alignment was disrupted by disturbing apical microtubules with nocodazole and by a BF-depleting Odf2 mutation. We constructed a theoretical model, which indicated that the apical cytoskeleton, acting like a viscoelastic fluid, provides a self-organizing mechanism in tracheal MCCs to align BBs linearly for mucociliary transport.

Introduction

The formation of mature epithelial sheets involves multiple steps in which epithelial cells adhere to each other to form a tight junction–based paracellular barrier, become polarized, and subsequently take on more specific differentiation states as they adopt the highly ordered structures required to elicit specific biological functions in vertebrates (Guillot and Lecuit, 2013; Rodriguez-Boulan and Macara, 2014; Tamura and Tsukita, 2014). How such complex processes are regulated is a fundamental question in cell biology and developmental biology.

Multiciliated cells (MCCs) are uniquely polarized to drive fluid transport in tissues by the synchronous beating and metachronal waves of hundreds of motile cilia on the apical membrane (Guirao and Joanny, 2007; Elgeti and Gompper, 2013). A differentiating MCC contains hundreds of basal bodies (BBs), which are short cylindrical structures at the base of mature cilia that are docked at the apical membrane (Anderson, 1972; Satir and Dirksen, 2011). In most types of MCCs, the orientation of the BBs, identified by their asymmetrically associated basal feet (BF), is precisely coordinated to support efficient mucociliary transport (Kunimoto et al., 2012; Chien et al., 2013).

The positional distribution of BBs (BB array) in the apical plane of MCCs depends on the cell type. For example, the BBs of ependymal MCCs in the brain exhibit unipolar clustering in the apical plane (Mirzadeh et al., 2010), whereas those of *Xenopus laevis* larval skin MCCs are evenly distributed throughout the entire apical region (Werner et al., 2011; Turk et al., 2015). Cytoskeletons are involved in regulating these systems, in which microtubules (MTs) are thought to synchronize BB orientation downstream of the planar cell polarity (PCP) core-protein functions (Vladar et al., 2012). Subapical actin is required for the proper distance between neighboring BBs (Werner et al., 2011), and myosin II activity plays a role in the unipolar migration of BB clusters (Hirota et al., 2010). However, the mechanisms involved in correctly assembling and maintaining the proper distribution of BBs on the cell surface remain to be fully elucidated.

In the present study, we examined mouse tracheal MCCs in which the BBs are linearly aligned, a pattern also found in oviduct MCCs. This striking pattern prompted us to address the mechanism by which these BBs become regularly aligned beneath the apical membrane. To follow BB pattern formation during MCC maturation, we developed a novel long-term and high-resolution live-imaging system in which cultured tracheal MCCs could be maintained as constantly moving specimens with beating cilia. We found that the development of the BB

The Rockefeller University Press $30.00
J. Cell Biol. Vol. 214 No. 5   571–586
www.jcb.org/cgi/doi/10.1083/jcb.201601023

JCB   571

THE JOURNAL OF CELL BIOLOGY

alignment pattern is highly dynamic and is achieved through a characteristic process, which we classified into four stereotypical patterns of BB array: "floret," "scatter," "partial alignment," and "alignment." Perturbing apical MTs caused the linear BB alignment pattern to revert to a floret-like pattern, and a genetic loss of BF that decreased MT density led to a failure to achieve BB alignment. Finally, we constructed a mathematical model for BB alignment based on an active hydrodynamic theory. This model showed the ability of cytoskeletal systems to self-organize BBs into specific patterns.

Results

The BB array adopts four stereotypical patterns during MCC differentiation, as revealed by long-term live imaging

In an individual MCC, BBs are generated via centrosome and deuterosome pathways and dock to the apical membrane to generate cilia (Stubbs et al., 2012; Zhao et al., 2013; Al Jord et al., 2014). When we examined the MCCs of adult mouse trachea and oviduct (Fig. S1 A), we found a strikingly linear BB alignment that was similar to the MCCs of cultured mouse tracheal epithelial cells (MTECs) prepared from the GFP-centrin2 transgenic mouse trachea (Fig. 1, A and B). To study the mechanism involved in BB alignment in the apical plane of MCCs, we developed a live imaging system that can be used for long periods (see Materials and methods for details). Using this system, we observed live GFP-centrin2–expressing MTECs (Higginbotham et al., 2004; Fig. 1, C–E) for 5–6 d, during which the differentiation of MCCs with beating cilia was unaffected (Fig. S1, E–H; and Video 1) and specimens in constant motion could be imaged.

Live imaging revealed that BBs first appeared as clusters with short cilia localized to the apical membrane (Fig. S1 B), which we termed the floret pattern. Subsequently, we found that BB florets scattered over the apical cell plane (scatter pattern) and neither clustered nor formed regular alignments. Then, around day 2, three to five neighboring BBs appeared to align with each other in a side-by-side fashion to form short lines (partial alignment pattern). By day 4, these short BB lines appeared to coalesce to form longer, parallel lines (alignment pattern; Fig. 1 E and Video 2). To quantitatively characterize these postciliogenesis BB arrays, we introduced an index of alignment (Ia), which has a high value when the BBs in a single cell are aligned (Fig. S1, C and D). Using Ia, we classified BB array patterns as follows: <0.22 (floret), 0.22–0.33 (scatter), 0.33–0.43 (partial alignment), and >0.43 (alignment; Fig. 1 F).

We next tracked the spatiotemporal dynamics of individual BBs by imaging GFP-centrin2. BBs in the floret pattern moved in and out of the area of the originally assigned floret cluster, and as a result, sets of BBs that later formed a line did not originate from a single floret (Fig. 2 A and Video 3). Over the course of MCC culture, the Ia value revealed a long-term ascending trend (Fig. 2 B), with a nearly constant number of BBs (Fig. 2 C). We found that the BBs moved most rapidly when they transitioned from the floret to the scatter pattern and then gradually slowed as they approached the alignment configuration (Fig. 2 D, left). After BB alignment was established, only minor changes occurred. We also observed occasional intermittent bursts of BB velocity caused by the large cellular deformation caused by the cell's reconnection with a neighboring cell
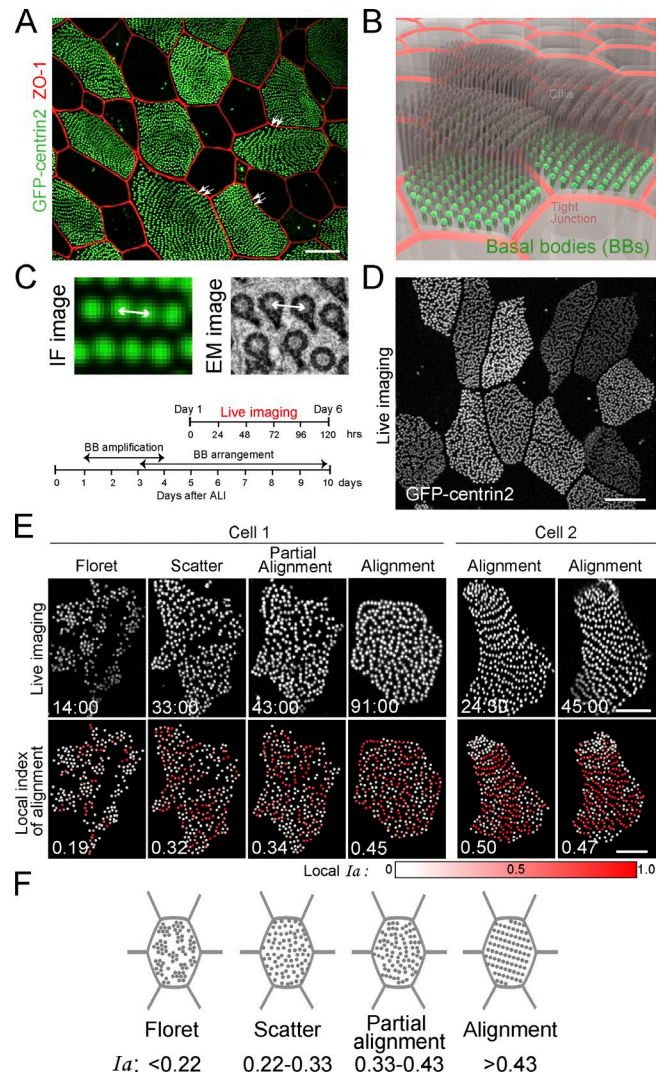

Figure 1. **Establishment of BB alignment during the MCC differentiation of MTECs revealed by long-term, high-resolution live imaging.** (A) Linear alignment of BBs (double arrows) in GFP-centrin2 MTECs at air–liquid interface (ALI) 21 d. (B) Illustration of mature polarized ciliated cells with linearly aligned BBs, depicted as green circles at the base of each cilium. (C) Immunofluorescence (IF) image of the GFP-centrin2 signal in BBs (top left, green), and electron micrograph (EM) image showing BBs (top right, black rings). Arrows, 200 nm. Timeline of live imaging and ALI culture (bottom). (D) GFP-centrin2 transgenic MTECs during live imaging. (E) Live imaging of GFP-centrin2 MTECs (see Video 2), which exhibited four BB patterns during BB-alignment development. The degree of alignment analyzed using the index of alignment (*Ia*) is shown as numeric values (E, bottom). Bar shows the range of local *Ia*s seen in the patterns. (F) Schematic drawing of representative live images showing each pattern. Bars, 5 µm.

(Fig. 2 D, right). Collectively, our live imaging system of MCCs with quantitative analyses revealed that the BB array adopted four stereotypical patterns, from a clustering floret pattern to a linear alignment during MCC differentiation.

The establishment of BB alignment is correlated with the refinement of BB orientation

Although earlier studies (Guirao et al., 2010; Werner et al., 2011) showed that the interplay between BB position and orientation underlies proper ciliary beating in *Xenopus* embryonic skin and mouse brain, little is known about this process in
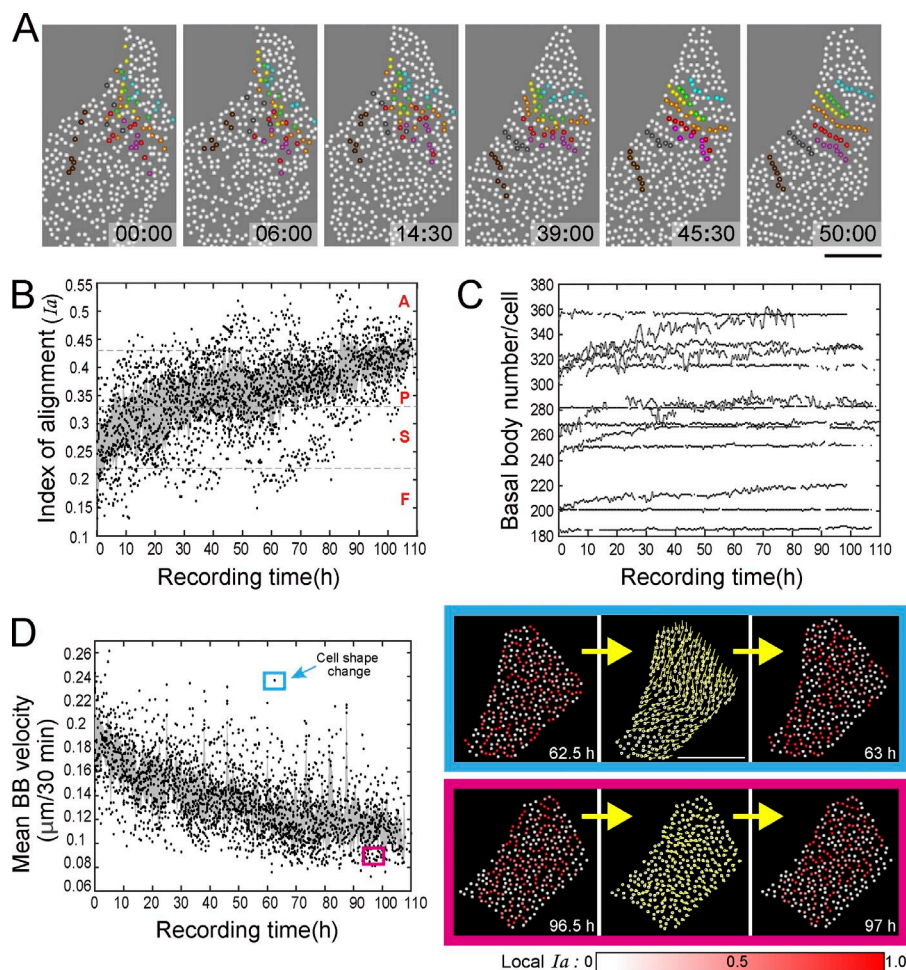
Figure 2. **Tracing the spatiotemporal dynamics of BBs.** (A) Migratory tracks of individual BBs recruited into eight alignments indicated by different colors. See Video 3. Time stamps shown are in hours:minutes. (B) Time course of BB alignment evaluated using Ia. A, alignment; P, partial alignment; S, scatter; F, floret. Horizontal dashed lines indicate boundaries that separate different patterns. (C) Number of BBs in individual cells during the development of BB alignment. The number of BBs remained almost constant during the stereotyped patterns of BB development. Note that apparent small fluctuations in BB numbers were caused by the fact that part of a cell was occasionally out of focus during the live imaging. (D) Temporal change in the velocities of BBs averaged within single cells (left). BB motion drifting caused by cell stretching (right, blue box) and BB motion under no significant cell deformation (right, pink box). Quantitative analyses in B–D were performed using the same cells ($n = 14$). Gray regions in B and D represent the 25–75 percentile band at each time point. Bars: (A) 5 µm; (D) 10 µm.

tracheal MCCs. We examined the development of tracheal BB orientation in the course of cell maturation and its correlation with BB alignment. By immunostaining Odf2 (Nakagawa et al., 2001) and centriolin (Gromley et al., 2003), which mark the positions of BBs and BF, respectively (Fig. 3 A and Fig. S2 A), we determined the orientation of each BB (Fig. 3, B and C), and then estimated the degree of uniformity of BB orientation by introducing the index of orientation (Io) (see Fig. S2 B and Materials and methods for details). During the progressive refinement of the BB orientation over time, the Io exhibited a rapid increase around air–liquid interface (ALI) days 6–7. The Io values taken from all of the samples exhibit a bimodal distribution, in which a group of cells with low (<0.3) Io values transitioned into cells with high (>0.7) Io values within 2 d. In the mouse trachea, cilia-generated directional fluid flow is absent at birth. At postnatal day 5, it is initially acquired rapidly within 48 h and reaches a plateau at postnatal day 9 (Francis et al., 2009). Because the BB orientation indicates the beating direction of the cilia, the bimodal Io values may correspond to the timing of fluid flow acquisition observed in the trachea.
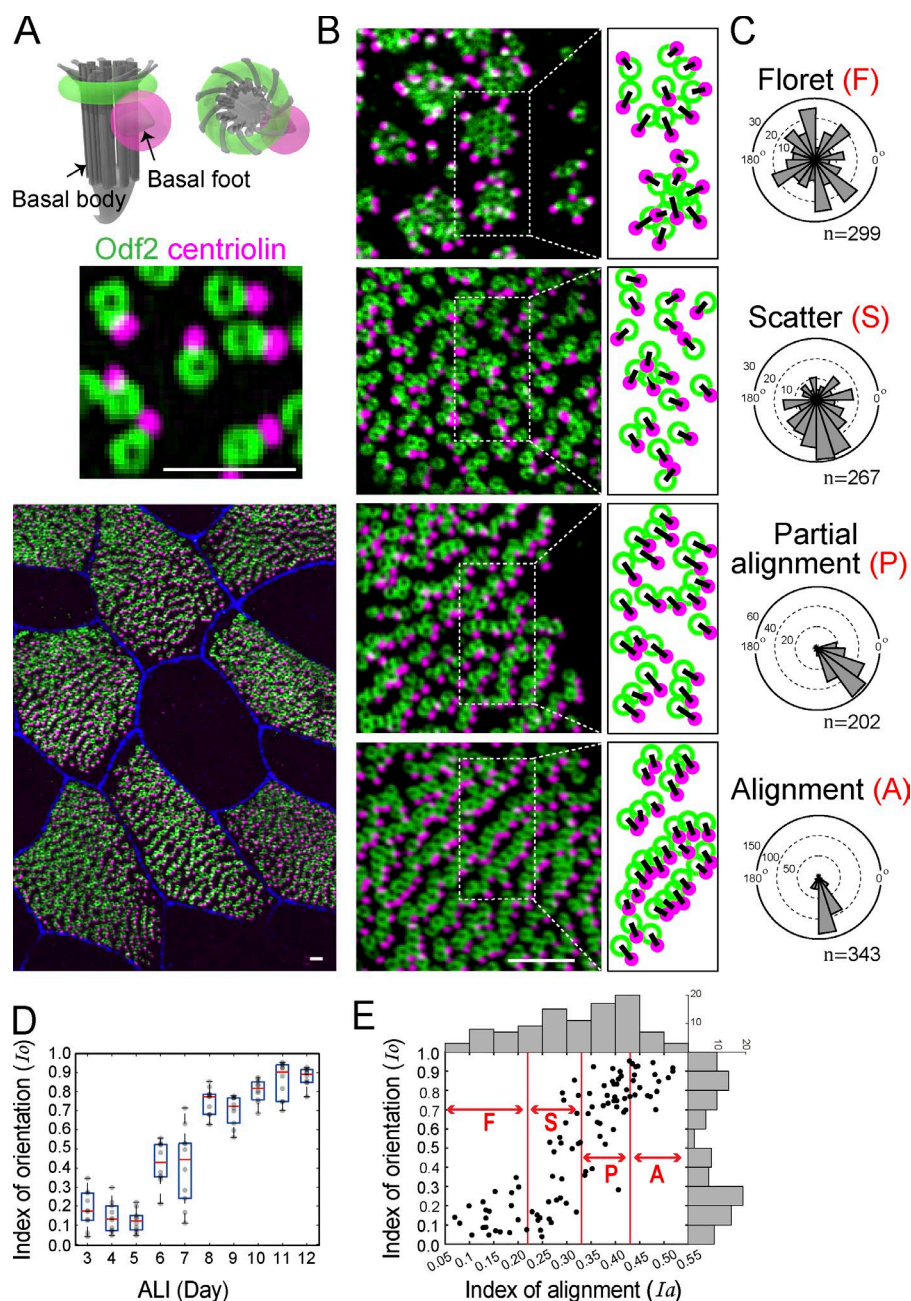
We also found a positive correlation between the alignment and orientation of BBs (Fig. 3 E). Specifically, $Ia > 0.25$ was coincident with the increase in Io. When Ia reached 0.4, Io was high ($Io > 0.8$). This relationship suggests a cooperative interaction between BB alignment and BB orientation. However, given that these analyses were based on fixed samples, the question remains whether BB alignment serves to facilitate the uniformity of BB orientations. Detailed investigations

are needed to address the causal relationship between BB alignment and orientation.

The apical cytoskeletons in MCCs change during BB alignment

BBs were reported to be associated with the apical cytoskeleton (Gordon, 1982; Sandoz et al., 1988; Werner et al., 2011; Antoniades et al., 2014), which may play a key role in the BB array formation. We examined the distribution of the apical actin filaments, intermediate filaments (IFs), and MTs in MCCs presenting the four patterns of BB arrays. For this purpose, we used a combination of super-resolution fluorescence microscopy (Fig. S2, C and D; and Fig. S3 A) and ultra–high-voltage electron microscopic tomography (UHVEMT) on thick sections (Fig. 4 A and Videos 4, 5, 6, and 7), and serial thin-section electron microscopy (Fig. S3 B). The apical surface of MCCs turned out to contain a mixture of cytoskeletons (actin filaments, IFs, and MTs), which form a dense polymer network confined to a thin layer just underneath the apical membrane (Fig. S2, C and D; and Fig. S3 A).

Actin filaments were distributed between BBs (Fig. S2 C); these filaments are known to run mainly downward from microvilli interspersed between cilia (Chailley et al., 1989; Pan et al., 2007). They occasionally appeared to be associated with BBs and BF, consistent with previous studies (Reed et al., 1984; Kunimoto et al., 2012) and with our electron microscopic observation of heavy meromyosin (HMM)–treated samples (Fig. 4 B). We found that IFs, which were not decorated with

Figure 3. **Interplay between BB alignment and orientation.** (A) Schematic drawing (top) and dual-color immunofluorescence for Odf2 and centriolin (middle and bottom), which marked the BB as a ring (green) and BF as a dot (magenta), respectively. Original image is shown in Fig. S2 A. (B) Representative immunofluorescence micrographs of each pattern, with an illustration showing a line from the center of the green ring to the center of the magenta dot. (C) Angle histograms of BB directions from representative cells in each pattern. (D) Boxplot of the dependency of the index of orientation (Io) on the ALI day ($n = 10$ cells/day). On each box, the red segment indicates the median, and the bottom and top edges of the box indicate the 25th and 75th percentiles, respectively. The whiskers extend to the lowest and highest data points, respectively. (E) Correlation between the linearity of the alignments and the uniformity of the directions during MCC differentiation. Each plotted point (black circle) represents a single cell in terms of its degree of BB alignment (horizontal axis, Ia) and orientation (vertical axis, Io). Histograms of Ia and Io are shown by gray bars. Immunofluorescence images of 100 cells with a total of 28,501 BB–BF pairs were analyzed. Bars, 700 nm.

HMM (a standard method for distinguishing them from actin filaments), were present between BBs, surrounding them at distances of ~50–100 nm (Fig. S2 E). Closer examination of the early-stage BB pattern revealed that thick bundles of IFs frequently appeared around the BB florets; this pattern was not reported previously (Fig. 4 A).

The number and distribution of MTs increased during the progressive reorganization of BB alignment. The MT density around BBs increased during the transition from the floret to scatter pattern (Figs. 4 A and S3 A). In the floret pattern, only a few MTs associated with BF in the apical cortical region of MCCs. In the scatter, partial alignment, and alignment patterns, significant numbers of MTs, distributed nearly in parallel to the apical membrane, were associated with BF (Figs. 4 A and S3 B). During the transition toward the alignment pattern, increasing numbers of MTs appeared to form parallel bundles through mutual interactions (Figs. 4 A and S3 C). Thus, in the apical

cortical layer containing the BBs, cytoskeletal structures were densely distributed, with some of them mutually interacting with BBs. Among these structures, the MTs were prominently aligned to promote BB alignment.

Actin and MT depolymerization affects BB alignment

To explore the role of the cytoskeleton in BB alignment, we treated MTECs with the actin depolymerizing agent cytochalasin D. We found that the alignment of BBs was disturbed and the spacing between BBs was decreased (Fig. S4 A), as well as dissociation of BBs from the apical membrane (Fig. S4 B). These observations are consistent with previous findings that actin plays an organizing role in BB spacing and apical docking (Pan et al., 2007; Werner et al., 2011; Antoniades et al., 2014). In addition, we noticed that cytochalasin D at a concentration that effectively disrupted the apical actin network, induced a
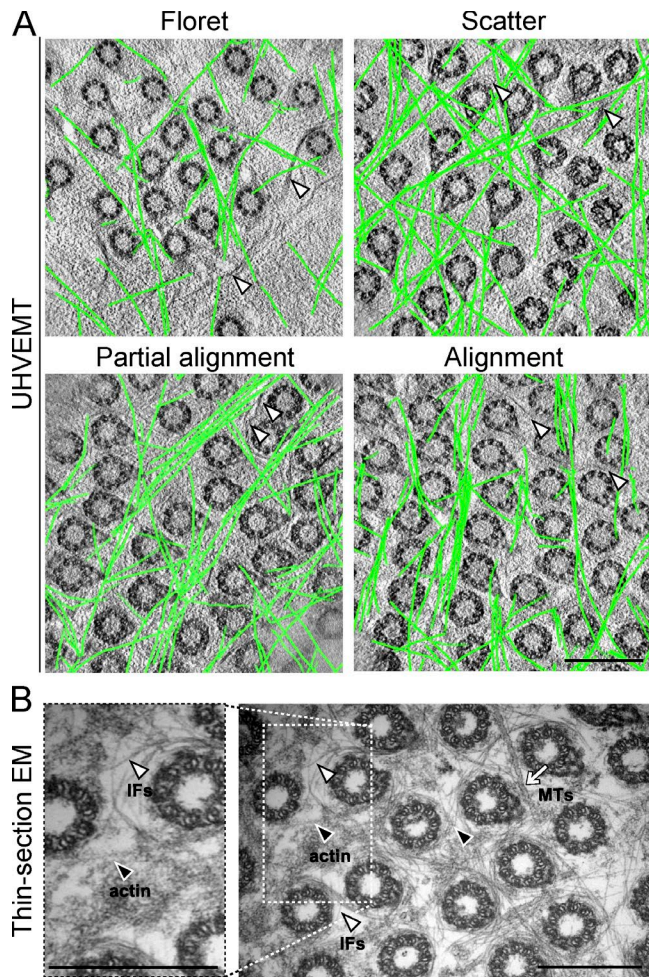
Figure 4. Apical cytoskeletons in MTECs revealed by UHVEMT and thin-section electron microscopy (EM). (A) Selected tomographic slices showing the pattern-specific distribution of MTs (green lines) and intermediate filaments (IFs; arrowheads). Note the thick bundles of IFs in the floret pattern. Microtubule lines were drawn from a 3D reconstruction and superimposed on a single cross section. See also Videos 4–8. (B) Thin-section EM image of HMM-treated MTECs at ALI 28 d (right). Actin filaments are decorated with HMM showing the typical arrowhead patterns (black arrowheads), whereas IFs are not decorated (white arrowheads). Arrow shows MTs. High-magnification image of actin filaments decorated with HMM (left). Bars, 500 nm.

shrinkage of the apical surface area in MCCs (Fig. S4 C) without significantly affecting the BB number (Fig. S4 D), resulting in a narrowing of the spacing between BBs. This observation suggests that actin determines BB positioning in an alternative way, not only by making interconnections at the proper distance between the BBs (Werner et al., 2011) but also by regulating the total area of the apical cell surface. A role for actin in regulating the apical surface area of MCCs was reported previously (Sedzinski et al., 2016).

MT depolymerization with nocodazole showed distinct effects on BB arrays. In GFP-centrin2–expressing MCCs in which the BBs were already aligned, nocodazole disturbed the BB alignment, resulting in clusters of BBs resembling the floret pattern (Fig. 5 A). The clusters of BBs were retained under an extended duration of MT depolymerization. On the other hand, washing out nocodazole remarkably returned the nocodazole-induced floret-like pattern to the partial alignment

pattern, suggesting that transitions between these states are reversible and MT dependent (Fig. 5, A and B; and Video 8). Furthermore, the response to nocodazole treatment differed depending on the state of BB alignment. The clusters of BBs were clearer on earlier-stage cells (Fig. 5 C), and the change in their I_a occurred more rapidly (Fig. 5 D). Because fewer MTs were associated with BBs in the floret pattern (Fig. 4 A), depolymerizing MTs in the earlier-stage cells would presumably lead to a more severe phenotype.

In nocodazole-treated cells, we confirmed that the immunofluorescent intensity of MTs was reduced (Fig. 5 E), whereas the actin filament distribution was relatively unaffected (Fig. S4 E). The networks of keratin IFs were profoundly altered by nocodazole, including the formation of filament bundles surrounding the floret-like BBs (Fig. 5, F and G). Similar morphological changes in IFs in response to shear stress have been reported in cultured human alveolar A549 epithelial cells (Flitney et al., 2009).
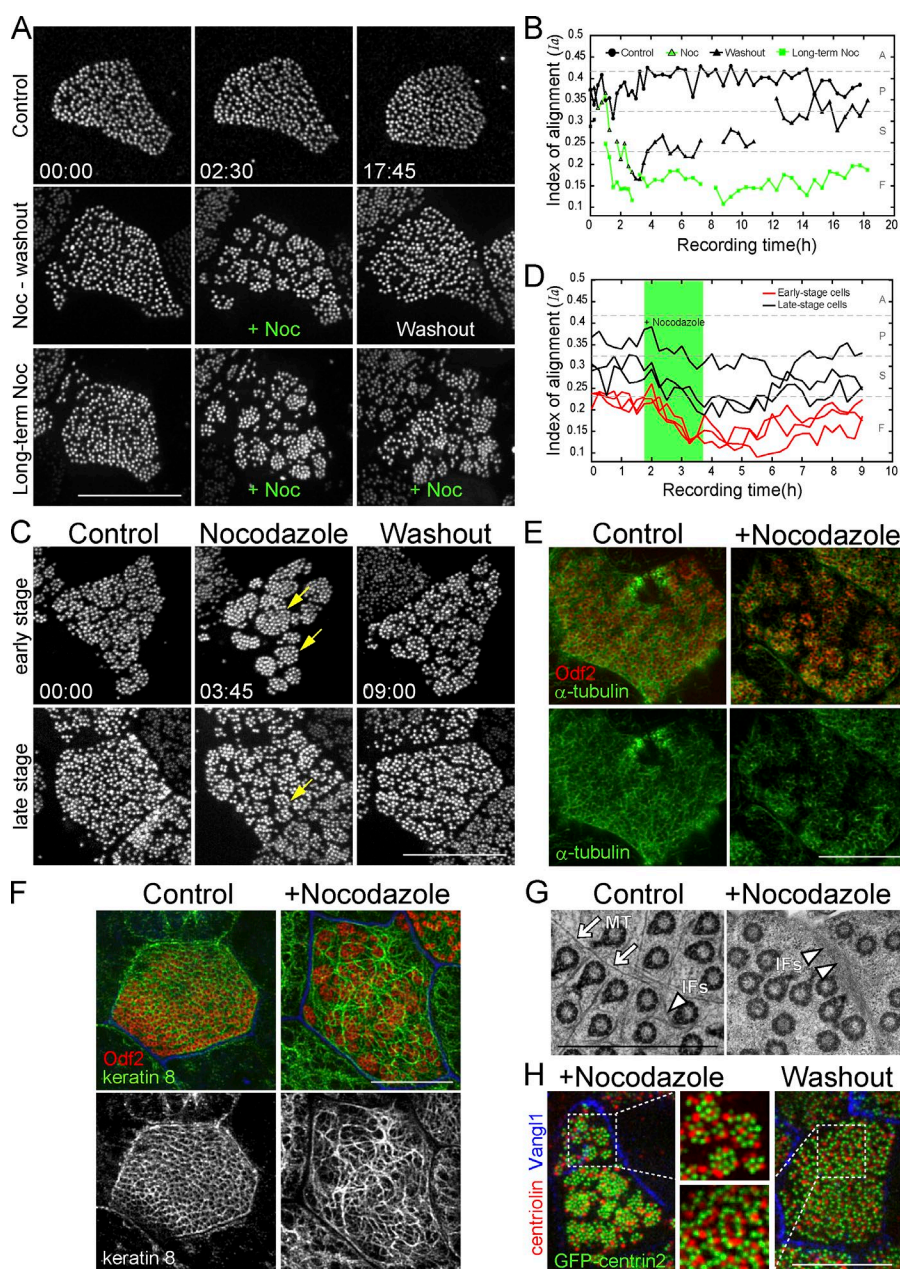
We also followed changes in BB orientation during nocodazole treatment using fluorescence of GFP-centrin2 and centriolin for BBs and BF, respectively (Fig. 5 H). We found that the coordination of the BB orientation was disturbed by MT perturbation, similar to the case in the floret pattern in BB arrays in the earliest phase of differentiation. Nocodazole washout restored the coordination of BB orientation.

Although these findings revealed that MTs play a critical role in the linear alignment of BB arrays from the floret to the partial alignment/alignment patterns, and in the simultaneous coordination of BB orientation, we could not exclude the participation of actin filaments and IFs in maintaining the proper BB arrays. The fact that MT disruption also affected the organization of keratin IFs suggests that the cytoskeletons interact with each other. To explore this possibility, we examined the localization of plectin, a major IF-based cross-linker protein that can facilitate physical interactions among MTs, IFs, and actin (Svitkina et al., 1996; Wiche et al., 2015). Although a previous study showed that the transcription level of plectin is up-regulated in the MCCs of MTECs (Hoh et al., 2012), the spatial distribution of plectin in the cells was not examined. We found that the distribution of plectin closely corresponded to that of keratin IFs (Fig. S5 A) and partly colocalized with MTs (Fig. S5 B). These findings support the idea that the three types of cytoskeletons associate with each other through crosslinkers like plectin and thus could act cooperatively to drive the dynamic motion of BBs.

Loss of BF from the BBs causes undirected BB movement and perturbs the establishment of the alignment pattern

Our previous work (Kunimoto et al., 2012) revealed the requirement of Odf2-based BF for functional mucociliary clearance. In the tracheal MCCs of Odf2 mutant ($Odf2^{\Delta Ex6,7\Delta Ex6,7}$) mice, the absence of BF impaired the regularity of the BB arrays and the polarized organization of apical MTs. However, the dynamic process of the BB array development in these mutant mice was unknown. To resolve this issue, we next examined MTECs prepared from GFP-centrin2-transgenic Odf2 mutant mice generated in this study, in which the BBs lack BF.

We detected BBs in the typical floret pattern in the $Odf2^{\Delta Ex6,7\Delta Ex6,7}$ GFP-centrin2 MTECs at the earliest stage of MCCs differentiation (Fig. 6 A and Video 8). Subsequently, and in sharp contrast to wild-type GFP-centrin2-MTECs (Figs. 1

Figure 5. **Requirement for MTs in establishing and maintaining BB alignment.** (A and B) Effects of nocodazole on the BB patterns in GFP-centrin2 MTECs. (A) Comparison of three different conditions of nocodazole treatment. Time in hours:minutes. (B) Measurement of *Ia* from cells shown in A. No treatment (black circles), short-term treatment (green triangles) followed by washout (black triangles), and long-term treatment (green squares). A, alignment; P, partial alignment; S, scatter; F, floret. (C and D) Different responses to nocodazole (Noc) treatment in early- versus late-stage cells. (C) More prominent clustering (arrows) appeared in the early-stage cells (top row) in the presence of nocodazole compared with late-stage cells (bottom row). See Video 8. Time stamps shown in hours:minutes. (D) Temporal changes in *Ia* in early- and late-stage cells. Black lines represent late-stage cells (those belong to scatter/partial alignment pattern), and red lines show early-stage cells (those belong to floret pattern). Green region indicates the period of nocodazole treatment. (E) Apical MTs in MTECs at ALI 6 d treated with 6.6 µM nocodazole for 2 h showed a lower intensity of α-tubulin staining compared with nontreated MTECs. (F) Immunostained images with an anti–keratin 8 mAb after nocodazole treatment revealed prominent keratin bundling. (G) Nocodazole treatment altered the normal IF network visualized by EM. Coincident with the depolymerization of MTs (white arrows), IFs (white arrowheads) formed thick bundles surrounding individual BB clusters. (H) The impaired BB pattern induced by nocodazole treatment was a floret-like pattern with random BB directions. Insets are magnified regions. Bars: (A, C, E, F, and H) 10 µm; (G) 1 µm.

E and 2 B), GFP-centrin2 in the BBs in *Odf2*$^{\Delta Ex6,7\Delta Ex6,7}$ MTECs revealed only a partial progression of the floret pattern to the scatter pattern and no progression to the partial alignment or alignment pattern. The dynamic behavior of the BBs was further specified by determining the *Ia*s, which remained low in the *Odf2*$^{\Delta Ex6,7\Delta Ex6,7}$ GFP-centrin2 MTECs (Fig. 6 B). In addition, tracheas from these mutant mice showed disorganized BB alignment (Fig. 6 C). These findings strongly suggest that BF-associated cytoskeletal structures, such as MTs, play important roles in BB alignment.

Mathematical modeling of the experimentally observed BB patterns

To obtain insight into the mechanisms underlying the BB patterns observed experimentally, we constructed a mathematical model for BB arrays based on the spatiotemporal dynamics of the apical cytoskeleton. The apical cytoskeleton is highly dynamic because of filament polymerization and depolymerization and because of the contractile stresses exerted by cytoskeletal motors such as myosin and kinesin. In addition, the cytoskeletal network behaves like a viscoelastic fluid (Jülicher et al., 2007) in the timescale relevant to multiciliated cell maturation (hours). Using this information, we developed a mathematical model for the formation of BB alignment based on active hydrodynamic theories describing the cytoskeleton (Marchetti et al., 2013; Prost et al., 2015). In our model, the apical cytoskeletons are treated as a two-dimensional viscous fluid that involves the activities of contractile force κ_c mediated by cytoskeletal motors, and filament polymerization with the rate κ_p. In this model, the BBs are regarded as objects that associate with the cytoskeletons by their BF (Kunimoto et al., 2012; Tateishi et al., 2013) and hence are transported by active cytoskeletal flows (Fig. 7 A and see Materials and methods) and are subject to random fluctuations in cytoskeletal motions.

Above a critical activity κ_c^* for a given κ_p, the contracting force leads to spontaneous pattern formation, classified as
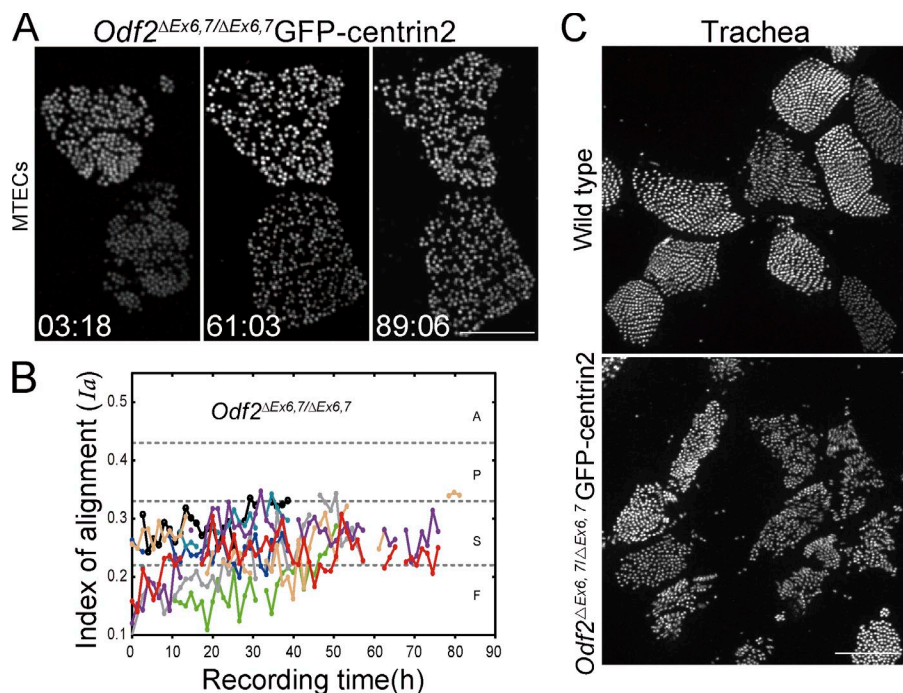
A $Odf2^{\Delta Ex6,7/\Delta Ex6,7}$ GFP-centrin2

MTECs

03:18   61:03   89:06

B

$Odf2^{\Delta Ex6,7/\Delta Ex6,7}$

Index of alignment (Ia) — A / P / S / F

Recording time(h)

C Trachea

Wild type

$Odf2^{\Delta Ex6,7/\Delta Ex6,7}$ GFP-centrin2

Figure 6. **BF are indispensable for BB alignment.** (A) Live imaging of $Odf2^{\Delta Ex6,7/\Delta Ex6,7}$ GFP-centrin2 MTECs in which the BBs lack BF. In the absence of BF, BBs transitioned from the floret to scatter pattern, but failed to develop into the alignment pattern. Stills are from Video 8, with time stamps shown in hours:minutes. (B) The Ia of eight cells from $Odf2^{\Delta Ex6,7/\Delta Ex6,7}$ GFP-centrin2 MTECs remained low. A, alignment; F, floret P, partial alignment; S, scatter. (C) Disorganized BB array observed in the $Odf2^{\Delta Ex6,7/\Delta Ex6,7}$ GFP-centrin2 tracheal cells lacking BF. The trachea was isolated from mice at postnatal 24 d. Bars, 10 µm.

spot, stripe, and intermediate patterns (Fig. 7 B). As the BBs associated with cytoskeleton via their BF were transported by cytoskeletal flows, BBs that settled into the cytoskeletal system under stripe-forming conditions exhibited sequential transitions from the floret through scatter and partial alignment and, finally, alignment patterns (Fig. 7 C and Video 9). In the earliest stage, in which the cytoskeleton was dilute, the BBs failed to associate with the cytoskeleton and were not advected by the flow, leading them to scatter from the florets via random walk. In contrast, in later stages, abundant cytoskeletal elements gave rise to spontaneous flows to form stripe arrays and hence to organize the BBs into alignment. These results correlated well with our experimental results of the characteristic patterning of BB arrays, which reached BB alignment through the four stereotypical patterns (Fig. 1, E and F).

The model also explained the cellular responses to perturbations observed in our experiments. Changing the model parameters to a lower polymerization rate and higher viscosity resulted in BB cluster formation (Fig. 7 D and Video 10), reminiscent of the nocodazole-induced clustering of BBs (Fig. 5 A). Our model analysis indicated that this clustering was attributed to two main events: (1) the lower polymerization rate shifted the cytoskeletal pattern from stripes to spots (Fig. 7 B); and (2) IFs were bundled after nocodazole treatment (Fig. 5, F and G), which stiffened the apical cytoskeletons and effectively increased their viscosity, resulting in slower and long-range flow (Mayer et al., 2010) that gathered many BBs to a large spot. At even lower polymerization rates (Fig. 7 E), the cytoskeleton no longer developed into any pattern and, accordingly, the BBs exhibited only the transition from floret to scatter via random fluctuations. This pattern was similar to the phenotype of Odf2 mutant cells, in which the apical MTs were not abundant (Kunimoto et al., 2012) and the BBs transitioned from floret to scatter but failed to develop into alignment (Fig. 6 A and Video 10). This model simulation explained our observations that nocodazole treatment and the genetic loss of BF perturbed the apical MTs to disturb the normal patterns of BB distribution and behavior.

Next, using this model, we examined how the conditions of the cytoskeleton at the cell boundary (the region in contact with a neighboring cell) affect the BB patterns within a single cell. This examination of boundary conditions was motivated by the observation that PCP molecules induce an asymmetric MT distribution at the cell membrane (Vladar et al., 2012; Shi et al., 2016) and that this biased distribution of MTs can guide BB alignment in a certain direction. To investigate how cytoskeletons along a boundary control BB patterns, we performed simulations in which the cytoskeletal velocity at the cell boundaries remained static (nonslip), which was based on our observation that the BBs move slowly at cell boundaries, and the cytoskeleton concentration was set as asymmetric along the long axis of a cell at an early stage of the simulation. The results shown in Fig. S5 C demonstrated that modifying the boundary conditions allowed for the precise control of the direction of BB lines in a direction perpendicular to the long axis of the cell. This model prediction is consistent with our experimental observations that an asymmetric MT distribution was established around the Floret stage (Fig. S5 D) and that the parallel BB alignments in a single cell were perpendicular to the long axis of the cell (Fig. S5 E).

Discussion

In the present study, we found that BB alignment in mature trachea and MTECs occurred through stereotypical changes in the BB array and that a self-organization mechanism involving the associated apical cytoskeleton could give rise to these patterns. The distribution patterns of BBs determined the positions of beating cilia, the biological significance of which has been widely studied in the context of synchronization and metachronality in the ciliary beating pattern (Werner et al., 2011; Brooks and Wallingford, 2014). Recent theoretical studies indicated that the pattern of ciliary positions affects the onset (Guirao and Joanny, 2007) and the efficiency
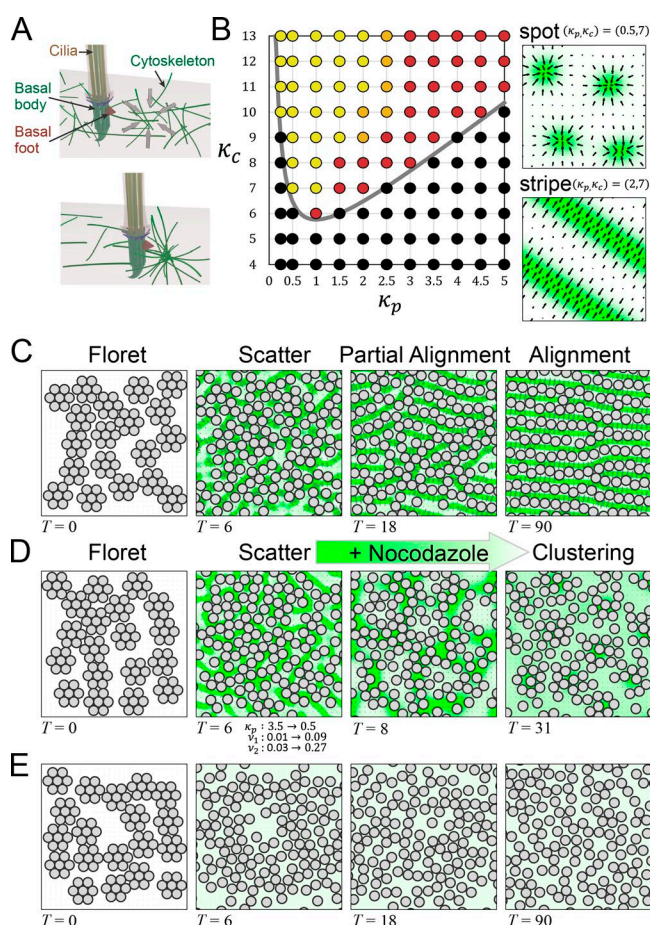
Figure 7. BB patterns are driven by dynamic remodeling of the apical cytoskeletons. (A) Model scheme. The cytoskeleton near the apical membrane (gray plane) is subject to contraction (gray arrows) by filament-bound motors and to diffusion and polymerization (top). BBs associated with the cytoskeleton through their BF are advected by cytoskeletal flows induced by filament reorganization (bottom). (B) Phase diagram showing the dependence of steady-state cytoskeletal patterns on κ_p and κ_c (left). The homogeneous state, spot pattern, and stripe pattern are represented by black, yellow, and red circles, respectively. Orange depicts a mixture of spots and stripes. Gray curve indicates the boundary separating the pattern-forming region $\kappa_c > \kappa_c^*$ and spatially homogeneous state $\kappa_c < \kappa_c^*$. Small arrows represent fluid velocities (right). Green indicates a high concentration of cytoskeleton and white indicates a low concentration (right). Fluid viscosities are $v_1 = 0.01$ and $v_2 = 0.03$. (C) Pattern evolution of the model system with a high polymerization rate of $\kappa_p = 3.5$ and 133 BBs (circles). The BBs, which were initially in the floret pattern, sequentially presented the scatter, partial alignment, and alignment pattern: $\kappa_c = 13$, $v_1 = 0.01$, and $v_2 = 0.03$. T is the simulation time. (D) Changing the model parameters as follows: κ_p: $3.5 \rightarrow 0.5$, v_1: $0.01 \rightarrow 0.09$, v_2: $0.03 \rightarrow 0.27$ at the scatter pattern ($T = 6$) induced BB clustering. (E) A low polymerization rate $\kappa_p = 0.1$ did not result in any pattern formation. All parameters except for κ_p were the same as in C. See also Videos 9 and 10.

of ciliary distribution, despite differences in the ciliary patterns of various cell types.

Here, we quantified the dynamic, sequential changes in ciliary patterns, which we termed floret, scatter, partial alignment, and alignment, that occurred during the maturation of mouse tracheal MCCs. Furthermore, we demonstrated that interactions between components of the apical cytoskeleton and BBs were crucial for establishing and maintaining these ciliary patterns; the genetic loss of BF in $Odf2^{\Delta Ex6,7\Delta Ex6,7}$ MTECs prevented BBs from achieving the alignment pattern, and drug-induced apical MT disruption caused the alignment pattern to change to a floret-like pattern. These changes in BB patterns were positively correlated with the refinement of ciliary orientation, indicating that ciliary alignment may have stabilized the unidirectionality of the BBs, to enhance the function of MCCs. The effects of other factors, such as cytoskeletal polarity (Shimada et al., 2006; Vladar et al., 2012), regulation by PCP signaling (Seifert and Mlodzik, 2007; Park et al., 2008; Mitchell et al., 2009; Boutin et al., 2014), and hydrodynamic coupling between cilia (Mitchell et al., 2007; Guirao et al., 2010; Matsuo et al., 2013) need to be examined in future studies.

Using our findings, we constructed a theoretical model for BB patterning driven by active reorganization of the apical cytoskeleton. This model reproduced the most prominent aspects of BB dynamics identified in our imaging analyses, including their spontaneous alignment during the normal development of MCCs in MTECs, their temporal clustering induced by nocodazole treatment, and their disordered pattern in the $Odf2^{\Delta Ex6,7\Delta Ex6,7}$ MTECs. Our model study also suggested that there is a joint effect between PCP regulation and cytoskeletal self-organization during the establishment of BB alignment. In terms of our simulation, PCPs define the boundary conditions of the system, which determine the directionality of the cytoskeletal pattern and BB alignment. These results provide mechanistic insight into the possible role of the cytoskeleton in establishing large-scale linear BB arrays in a cell sheet. Together, our experimental and theoretical studies highlight a possible biological function of the apical cytoskeleton in tracheal MCCs in the linear alignment of cilia, as a typical example of the terminal differentiation of epithelial cell sheets.

Self-organized cytoskeletal patterns are relevant in many biological functions, such as spindle body formation, in which motor-mediated interactions between MTs determine the viscoelastic nature of the spindle (Shimamoto et al., 2011; Brugués and Needleman, 2014). Self-organized cytoskeletal mechanisms are also suggested to be involved in apical structure formation (Chaudhuri et al., 2011; Gowrishankar et al., 2012). The model of BB alignment and the apical cytoskeleton in tracheal MCCs set forth here was based on the apical cytoskeleton as a dynamic material with cytoskeleton-dependent viscosity. Although different BB distributions in the apical layer have been reported in various organ systems, some common mechanisms may be involved in the formation and regulation of BB organization. Our present study provides a new framework for understanding apical cytoskeletal function as exemplified in multiciliated epithelial cells. Such an autonomous, self-organizing mechanism with or without a coupled cell signaling system may play critical

of fluid transport (Osterman and Vilfan, 2011; Elgeti and Gompper, 2013) through the coordination of synchronized or metachronal ciliary beating. On the other hand, very few studies have addressed the physical mechanism underlying the establishment of the cilia positioning itself. Previous studies in *Xenopus* (Werner et al., 2011) and mouse brain (Boutin et al., 2014) demonstrated that the cytoskeleton is a common key player responsible for the formation and regulation

roles in various morphogenetic processes in both single-cell and multicellular systems.

Materials and methods

Animals

All procedures involving animals were approved by the institutional animal care and use committee of Osaka University. The mice used in this study included GFP-centrin2 (Higginbotham et al., 2004), wild-type C57BL/6J (CLEA Japan), and $Odf2^{\Delta Ex6,7\Delta Ex6,7}$ GFP-centrin2. To generate $Odf2^{\Delta Ex6,7\Delta Ex6,7}$ GFP-centrin2 mice, homozygous GFP-centrin2 mice were crossed with $Odf2^{flox/+}$ mice to produce male $Odf2^{flox/+}$ GFP-centrin2 mice. Then, the latter were intercrossed with female $CAG^{Cre/+}$; $Odf2^{flox-del/+}$ mice to generate $Odf2^{\Delta Ex6,7\Delta Ex6,7}$ GFP-centrin2 mice. The protocols for genotyping were described previously (Kunimoto et al., 2012).

Primary culture of tracheal cells and long-term live imaging

MTEC cultures were prepared from the trachea of mice at 7–10 wk of age as described previously (You et al., 2002), with replacement of the conventional medium. To improve the cell yield, enzymatic digestion was performed with gentle shaking at 4°C for 16–20 h. This method routinely yielded ~1.08×10^6 cells/ml from four mice, which was sufficient for 20 transwell 24-well filters (Corning). The enzymatic digestion was stopped by adding FBS (Cell Culture Bioscience) to the cell suspension at a final concentration of 10%. Cells were pooled by centrifugation at 400 g for 10 min at 4°C, then resuspended in MTEC Basic Medium (You et al., 2002) with 10% FBS for 3.5 h at 37°C, 5% CO_2 to adhere contaminating fibroblasts. Nonadherent cells were then collected by centrifugation, counted, and seeded at 10^5 cells/cm² onto polyester transwell filters (Corning) coated with 50 µg/ml collagen type I (Corning). The proliferation stage was maintained using the commercially available BEGM BulletKit (CC-3170; Lonza). The ALI stage was created after 4 d of culture using PneumaCult (05001; STEMCELL Technologies) according to the manufacturer's instructions. For live imaging, transwell filters with a MTEC sheet (ALI 5–6 d) were cut out from the plastic support and inverted (cell side facing down) onto a glass-bottomed dish (D11140H; Matsunami Glass). Medium was supplied from an additional chamber attached to the back surface of the inverted insert. The medium was changed every other day.

Inhibitor experiments and HMM treatment

Inhibitor experiments were performed either during live imaging or under normal incubation conditions. For MT depolymerization, 6.6 µM nocodazole (Sigma-Aldrich) was applied to MTECs at ALI 6 d for 2 h, then replaced with 500 µl of fresh medium for recovery. For actin depolymerization, 10 µM cytochalasin D (Sigma-Aldrich) was used at ALI 7 d for 5–10 h.

To permit HMM to diffuse into the cells, MTECs at ALI 28 d were incubated with 0.1% Triton X-100/0.01 µM paclitaxel in PHEM buffer (60 mM Pipes, pH 6.9, 25 mM Hepes, pH 6.9, 10 mM EGTA, and 2 mM $MgCl_2$) for 15 min, then washed with PHEM buffer. Freshly thawed rabbit HMM solution was dialyzed against PHEM buffer at a final concentration of 1 mg/ml. The cells were then incubated with this HMM solution and 0.01 µM paclitaxel for 1 h at RT, washed, and fixed for thin-section electron microscopy.

Indirect immunofluorescence

MTECs and whole-mount trachea and oviduct were fixed in cold methanol (−20°C) or 4% PFA in Hepes-buffered saline (RT), permeabilized with 0.2% Triton X-100/PBS for 5 min (RT), and then incubated in 1% BSA/PBS for 30 min (RT). Incubations with primary and secondary antibodies were performed for 1 h each (RT). The following primary antibodies were used: rabbit anti-Odf2/Cenexin (1:500; Abcam), mouse anti–α-tubulin (1:500; Sigma-Aldrich), rabbit anti-Vangl1 (1:500; Sigma-Aldrich), rabbit anti–ZO-1 (1:500; Invitrogen), rat anti-Odf2 (Tateishi et al., 2013), rat anti–centriolin (Ishikawa et al., 2005), mouse anti–ZO-1 (T8-754; Kitajiri et al., 2004), rabbit anti–plectin 1 (1:100; Abcam), and mouse anti–keratin 8 (provided by A. Hirako and K. Owaribe, Nagoya University, Nagoya, Japan) antibodies. Secondary antibodies (1:500) included rat anti-GFP (Invitrogen) and species-specific Alexa Fluor 488, 568, and 647 (Invitrogen) antibodies. Rhodamin-conjugated phalloidin was purchased from Invitrogen.

Microscopy

Live imaging and confocal microscopy. BB movement was recorded using a Spinning Disk-Olympus super-resolution microscope (SD-OSR; Olympus; Hayashi and Okada, 2015) equipped with a silicon oil-immersion objective lens (UPlanSApo 60× Sil, NA 1.3; Olympus), a sCMOS camera (ORCA-Flash 4.0 v2; Hamamatsu Photonics), appropriate filter sets for DAPI/FITC/TRITC, a motorized scanning deck, and an incubation chamber (37°C; 5% CO_2; 85% humidity; Tokai Hit). The recording was performed by multistage acquisitions with 10–30 fields of view, each covering ~10 cells/field. Time intervals were 30 min for long-term recording, 15 min under nocodazole treatment, and 1–2 h under cytochalasin D treatment. Image acquisition was set to z-series of 8–12 planes with a 0.5-µm distance. Immunofluorescently stained samples were imaged using a silicon oil-immersion objective lens (UPlanSApo 60× Sil, NA 1.3; Olympus) and 1.6× conversion lens. All hardware was controlled with MetaMorph (Molecular Devices). The resulting 3D images were converted into 2D images by maximum intensity projection in the z-direction before the image analysis necessary for detecting BBs and BF.

Thin-section electron microscopy and electron tomography with UHVEMT. MTECs were fixed with 2.5% glutaraldehyde and 2% PFA at 37°C for 1 h. The following steps were based on classical methods for sample preparation for electron microscopy (Ishikawa et al., 1969). Serial sections of 90 nm were cut on an ultramicrotome (Ultracut E; Leica Biosystems) and stained with uranyl acetate and lead citrate for double contrasting. Image observation was performed using a JEM 1400-Plus (JEOL). For observation using UHVEM Tomography, 700-nm-thick section specimens were observed using an ultra–high-voltage electron microscope operating at 1 MeV (H-3000; Hitachi). The images were acquired at 25,000 times from −60° to +60° at 2° intervals around a single-axis tilt series, as described previously (Kunimoto et al., 2012).

Cilia beating. Cilia beating was recorded using a high-speed camera (FASTCAM MC2.1; Photron) connected to an upright microscope (Axioplan; ZEISS) with 63× objectives.

Image analysis

Index of alignment Ia. To quantify the degree of alignment in BB configurations, we constructed the index of alignment Ia (Fig. S1 D). Ia is calculated from the given positions of BBs in a single cell, $r_i(i = 1, ..., N)$, by the following three steps.

Step 1: Determination of neighboring BBs. BBs whose positions were within a range of 1.3d from r_i were determined to be neighbors of the ith BB. Here, d represents the diameter of the BBs, and we set $d = 4$ pixels. Note that the distance from a BB to its second-nearest BBs in a square lattice is $\sqrt{2}\,d \sim 1.4d$, and our choice of 1.3d allows us to exclude the second-nearest BBs from the neighboring BBs of a given BB.

Step 2: Local evaluation of the alignment. For every ith BB with n neighbors, the local index of alignment, Ia,i, was evaluated using the following set of equations:

If $n = 2$ or 3
$$\begin{cases} I_{a,i} \equiv \dfrac{\sum_{k>j}^n \sum_{j=1}^{n-1}\left[W_{jk}L(\phi_{jk})\right]}{\sum_{k>j}^n \sum_{j=1}^{n-1} W_{jk}} \\[2mm] L(\phi_{jk}) \equiv \max_{0\le\phi_{jk}\le\pi}\left(-\cos\phi_{jk},0\right) \\[2mm] W_{jk} \equiv w_j w_k \\[2mm] w_l \equiv \min_{0\le|r_l-r_i|\le 1.3d}\left[1-\dfrac{(|r_l-r_i|-d)}{(1.3d-d)},1\right] \end{cases},$$

where ϕ_{jk} is the acute including angle between the vector $r_j - r_i$ and $r_k - r_i$. The linearity function L has high values (~ 1) for only linearly aligned BBs ($\phi_{jk}\sim\pi$) and acts as a filter to distinguish aligned patterns from other configurations. The weight function w was used to increase the effect of the closer BBs within the neighborhood.

If $n \ge 4$, then we set $Ia,i = 0$. If $n = 1$, we performed the following process. Let j be the label of the single neighboring BB of the ith BB. If the jth BB has two neighboring BBs, then we define $Ia,i = Ia,j$, by which the BBs at the edge of the line have a high value. If the number of neighbors of the jth BB is 1 or more than 3, we define $Ia,i = 0$.

Ia,i is bounded in the interval [0, 1] with 1 indicating highly aligned patterns of BBs and 0 indicating nonlinear configurations.

Step 3: Averaging. Finally, the index of alignment Ia was defined as the mean of Ia,is of the BBs within a single cell:

$$Ia \equiv \frac{1}{N}\sum_{i=1}^N I_{a,i}.$$

Index of orientation Io. To measure the variation in basal foot orientations within a single cell, we introduced the index of orientation Io (Fig. S3 B). Io is calculated as follows. Suppose we have a set of vectors, each of which originates from the center of a BB and ends at its accompanying BF. We denote the angle between each vector and the horizontal axis by $\theta_i (i = 1, ..., N)$, where N represents the total number of BBs within a single cell. The θ_is were first transformed into unit vectors in two-dimensional p_is by

$$p_i = (\cos\theta_i, \ \sin\theta_i).$$

After this transformation, a single mean vector p was computed by

$$p = \frac{1}{N}\sum_{i=1}^N p_i.$$

The index of orientation Io is defined as $Io \equiv |p|$. Note that Io is bounded in the interval [0, 1]. Io is an indicator of the spread of BF orientations, θ_i. If all BF point in the same direction, Io will be 1. If the BF orientations are random, Io will be 0.

For comparison, Fig. S3 B shows the Io values calculated for five representative angle datasets illustrated by rose diagrams, which are commonly used to represent BF orientations (Chien et al., 2013).

Mathematical model of BB alignment

Hydrodynamic description of the apical cytoskeleton. In short timescales (seconds), the cytoskeleton behaves like an elastic solid, but in the longer timescales relevant to BB alignment (hours), it acts like a viscous fluid because of the polymerization/depolymerization and motor-induced dynamic remodeling of cytoskeletal filaments. Several theoretical studies modeling the cytoskeleton as an active viscous fluid have been successfully applied to a wide range of biological systems, including muscle sarcomeres (Banerjee and Marchetti, 2011), moving cells (Shao et al., 2012), the contractile ring (Salbreux et al., 2009), the cell cortex (Rauzi et al., 2010), and the metaphase spindle (Brugués and Needleman, 2014). In the following analysis, we based our mathematical model on the description of the apical cytoskeleton as an active fluid.

Because the apical surface is very thin compared with the other dimensions of the whole cell, we restricted our model to two dimensions. We described the apical cytoskeleton dynamics using two continuum fields: fluid velocity v(x,t) and cytoskeleton concentration C(x,t), where x(x,y) represents the apical xy-plane coordinates and t is the time. We did not distinguish between the components of the apical cytoskeleton, i.e., actin filaments, IFs, and MTs. This assumption was supported by our experimental observations of plectin localization (Figs. S5, A and B), which suggested that complex interactions occur among the apical cytoskeletons during the progression of BB alignment and that these interactions cause the different cytoskeletons to have cooperative dynamics, behaving like a single fluid entity on a long timescale. In general, filament orientation is thought to play an important role in cytoskeletal pattern formations (Marchetti et al., 2013), and the concentration C(x,t) alone does not describe all of the properties of the cytoskeleton. In this study, however, the minimal model in which the apical cytoskeleton is described by the concentration C(x,t) and velocity v(x,t) was able to capture the most prominent aspects of BB dynamics, including the aggregation induced by nocodazole treatment, the disordered patterns in Odf2 mutant cells, and the spontaneous alignment during normal development.

Because of the low Reynolds number at the cellular length scale, the fluid acceleration is negligible compared with viscosity. Under this condition, the force balance equation is given by

$$\nabla \cdot \sigma = \gamma v. \tag{1}$$

The left-hand side of Eq. 1 is the force acting on the fluid, whereas the right-hand side represents the friction between the cytoskeletal network and the penetrating cytosol. Although the friction coefficient γ depends on the microscopic environment between the cytoskeleton and cytosol, we treat γ as a constant. The stress tensor, σ, is composed of passive and active parts as

$$\sigma = \sigma_p + \sigma_a. \tag{2}$$

The passive contribution is given by

$$\sigma_p = \eta\left[\nabla v + (\nabla v)^T - \frac{2}{d}(\nabla \cdot v)I\right] + \lambda(\nabla \cdot v)I, \tag{3}$$

where η and λ are shear and bulk viscosities arising from internal friction in the cytoskeleton, $d(= 2)$ is the space dimension, and I is the unit tensor. The active contribution, σ_a, originates from the contractile forces exerted by molecular motors, like kinesin and myosin, bound to the cytoskeleton. We chose σ_a as a simple isotropic contraction:

$$\sigma_a = m \cdot \mu F(C)I. \tag{4}$$

Here, m is the concentration of motors bound to the cytoskeleton. Provided that the motor diffuses sufficiently rapidly, the motor concentration is assumed to be uniform. σ_a describes the change in chemical potential because of the hydrolysis of ATP by a motor, and $F(C)$ is the duty ratio of motors and is given by

$$F(C) = \frac{k_{on} C}{k_{off} + k_{on} C}, \tag{5}$$

where k_{on} and k_{off} are, respectively, the binding and unbinding rates according to first-order reaction kinetics.

To complete the continuum description, we need equations describing the dynamics of the cytoskeleton concentration C. Because C obeys the conservation law with concentration flow j and reaction $R(C)$, we obtain

$$\frac{\partial C}{\partial t} = \nabla \cdot \mathbf{j} + R(C). \tag{6}$$

The form of the concentration flow j is

$$\mathbf{j} = C\mathbf{v} - D\ \nabla\ C. \tag{7}$$

The first term in the right-hand side of Eq. 7 is the flow arising from advection by the fluid. The second term represents the diffusive flow with diffusion coefficient D. The reaction term $R(C)$ consists of polymerization and depolymerization processes:

$$R(C) = k_p - k_d C, \tag{8}$$

where k_p and k_d are, respectively, the polymerization and depolymerization rates of the cytoskeleton. Eqs. 1–8 lead to the final form of the equations describing the apical cytoskeleton as

$$\eta\,\nabla^2 \mathbf{v} + \lambda\ \nabla\ (\nabla \cdot \mathbf{v}) + k_c\ \nabla\ \left(\frac{C}{C_s + C}\right) - \gamma \mathbf{v} = 0$$

and

$$\frac{\partial C}{\partial t} = D\nabla^2 C - \nabla \cdot (C\mathbf{v}) + k_p - k_d C,$$

where $k_c = m \cdot \mu$ is the effective contraction strength and $C_s \equiv k_{off}/k_{on}$ is the saturation concentration.

Dynamics of the BB. Based on a previous study (Kunimoto et al., 2012) showing that the BF associate with apical MTs, we modeled BBs as hard "particles" that associate with the apical cytoskeleton via their accompanying BF and hence are advected by the cytoskeletal flow. For simplicity, we assumed that each BB is a circular object with radius r and that the motion of the BBs does not affect the cytoskeleton and is completely determined by the cytoskeletal fluid velocity v. The steric interaction that prevents BBs from merging can be modeled by using a repulsive force acting on overlapping BBs as:

$$\mathbf{F}_i^{BB} = -\sum_j k_s \left(\left|\mathbf{X}_i - \mathbf{X}_j\right| - 2r\right) \frac{\mathbf{X}_i - \mathbf{X}_j}{\left|\mathbf{X}_i - \mathbf{X}_j\right|} \text{ if } \left|\mathbf{X}_i - \mathbf{X}_j\right| < 2r,$$

where $\mathbf{X}_i$ represents the position of the ith BB and k_s is the strength of the steric interaction. To prevent the penetration of cytoskeleton into the BBs, we consider another repulsive force acting between the cytoskeleton and BBs, of the form $\mathbf{F}_i^{BC} = -k_r \overline{\nabla C}$, where $\overline{\nabla C}$ is the spatial mean of the concentration gradient inside the ith BB. Our experimental data showing that not all BF associate with MTs suggest that the interaction between the cytoskeleton and each BF is stochastic. To take this effect into account, a random variable ξ following a normal distribution is added to the flow-advected motion of the BBs. The statistics of ξ can be written as $\xi(t) = 0$ and $\xi(t) \otimes \xi(t') = A\delta(t - t')\mathbf{I}$, where the angle brackets $\langle \cdots \rangle$ denote an ensemble mean, and δ is the delta function. A represents the amplitude of fluctuation.

To summarize, the time evolution of the position of the ith BB $\mathbf{X}_i$ is described by

$$\frac{d\mathbf{X}_i}{dt} = \bar{v} + \mathbf{F}_i^{BB} + \mathbf{F}_i^{BC} + \xi,$$

where $\bar{v}$ is the spatial mean fluid velocity inside the ith BB.

Nondimensionalized form model equations. To obtain a set of core parameters, we nondimensionalize the model equations as

$$v_1 \nabla^2 \mathbf{u} + v_2\ \nabla\ (\nabla \cdot \mathbf{u}) + \kappa_c\ \nabla\ \left(\frac{c}{1 + c}\right) - \mathbf{u} = 0, \tag{9}$$

$$\frac{\partial c}{\partial \tau} = \nabla^2 c - \nabla \cdot (c\mathbf{u}) + \kappa_p - c, \tag{10}$$

and

$$\frac{d\mathbf{R}_i}{d\tau} = \bar{u} + \mathbf{G}_i^{BB} + \mathbf{G}_i^{BC} + \zeta \tag{11}$$

by introducing the following scale transformations:

$$\tau \equiv k_d t, \mathbf{r} \equiv \sqrt{\frac{k_d}{D}}\mathbf{x}, c \equiv \frac{C}{C_s}, \mathbf{u} \equiv \frac{1}{\sqrt{k_d D}}\mathbf{v}, \mathbf{R}_i \equiv \sqrt{\frac{k_d}{D}}\mathbf{X}_i$$

$$\mathbf{G}_i^{BB} = -\sum_j \kappa_s \left(\left|\mathbf{R}_i - \mathbf{R}_j\right| - 2\rho\right) \frac{\mathbf{R}_i - \mathbf{R}_j}{\left|\mathbf{R}_i - \mathbf{R}_j\right|} \text{ if } \left|\mathbf{R}_i - \mathbf{R}_j\right| < 2\rho$$

$$\mathbf{G}_i^{BC} = -\kappa_r \overline{\nabla c}$$

$$\zeta(\tau) = 0$$

$$\zeta(\tau) \otimes \zeta(\tau') = \alpha\delta(\tau - \tau')\mathbf{I}$$

and dimensionless parameters

$$v_1 \equiv \frac{\eta k_d}{\gamma D}, v_2 \equiv \frac{\lambda k_d}{\gamma D}, \kappa_c \equiv \frac{k_c}{\gamma D}, \kappa_p \equiv \frac{k_p}{k_d C_s},$$

$$\kappa_r \equiv \frac{k_r C_s}{D}, \kappa_s \equiv \frac{k_s}{k_d}, \rho \equiv \sqrt{\frac{k_d}{D}}r, \alpha \equiv \frac{1}{k_d D}A.$$

The variables and parameters of the model are summarized in Table 1.

Detection of BBs and BF

We used least-squares fitting to identify the positions of the BBs and BF in the immunofluorescence images. The fitting algorithm proceeded as follows.

Step 1. The fluorescence image of the BBs (BF) was normalized to scale the intensity between 0 and 1, and the fitting-error function E was calculated by

$$E(m_c, n_c) = \sum_{m,n} W(m - m_c, n - n_c)\left[I(m,n) - I_t(m - m_c, n - n_c)\right]^2, \tag{12}$$

where W, I, and I_t are, respectively, the weight function, the normalized fluorescent image of the BBs (BF), and the target image. m and n are pixel indices. m_c and n_c represent the centers of the BBs (BF), which will be identified in step 2. The summation in Eq. 12 runs over the image I. W and I_t were specified as

$$W(m,n) = \frac{1}{2}\left[1 + \tanh\left(\frac{a - \sqrt{m^2 + n^2}}{b}\right)\right]$$

$$I_t(m,n) = \begin{cases} \left[1 - H\exp\left(-\frac{m^2 + n^2}{2\sigma_b^2}\right)\right] W(m,n) & \text{for the BB} \\ \exp\left(-\frac{m^2 + n^2}{2\sigma_f^2}\right) & \text{for the BF} \end{cases},$$

where a, b, H, σ_b, and σ_f are the parameters characterizing the shape of a BB (BF). In the present study, we set $a = 5$ (pixel), $b = 1$ (pixel), $H = 0.75$, $\sigma_b = 2$ (pixel), and $\sigma_f = 2$ (pixel).

Step 2. Because E takes local minima at the positions of the BBs (BF), one can find the most likely positions of the BBs (BF) by detecting all of the minima of E. For this purpose, the right-hand side of Eqn. (S1) was rearranged using two-dimensional discrete convolution to obtain

$$E(m_c, n_c) = I^2 * W - 2I * (WI_t) + 1 * (WI_t^2), \tag{13}$$

where

$$f*g \equiv \sum_{m',n'} f(m',n')g(m'-m,n'-n)$$

represents the two-dimensional discrete convolution. Using Eq. 13, all of the pixel indices (m_c, n_c) whose values of $E(m_c, n_c)$ were lower than a threshold value E^* and smaller than those of their 8 nearest neighbors were extracted to identify all of the minima of E, i.e., the positions of the BBs (BF). We set $E^* = 5$.

Step 3. All false-positive and false-negative detections were manually corrected.

BB–BF pairing algorithm

In the analysis of immunofluorescence images, individual BF needed to be correctly paired with their host BBs. To accomplish this, we applied a nearest-neighbor-pairing method, because each BF can be regarded as the nearest object of its host BB. The method we used was originally introduced by Labonté (1999) and improved later by Ohmi (2008).

The method is implemented in an iterative manner, as described in the following steps:

Step 1. Let $r_i(i = 1, ..., N)$ and $q_j(j = 1, ..., M)$ respectively be the two-dimensional coordinate vectors of the ith BB and the jth BF within a single cell. $N(M)$ is the total number of BBs (BF). First, the weight vector α_i was assigned to r_i and β_j was assigned to q_j, and they were initialized as

$$\alpha_i^{[k]} \leftarrow r_i \; (i = 1, \cdots, N), \quad \beta_j^{[k]} \leftarrow q_j \; (j = 1, \cdots, M), \; k \leftarrow 0,$$

where the superscript $[\cdot]$ indicates the iteration number.

Step 2. Next, the weight vector α_i was subjected to the following change:

$$\alpha_i^{[k+1]} \leftarrow \alpha_i^{[k]} + \sum_{j=1}^{M} \Delta\alpha_i^{[k]}(c_j)$$

$$\Delta\alpha_i^{[k]}(c_j) = \Gamma_i^{[k]}\left(\beta_j^{[k]} - \alpha_{c_j}^{[k]}\right),$$

where c_j denotes the index of the BB whose weight vector $\alpha_i^{[k]}$ was closest to $\beta_j^{[k]}$, and $\Gamma_i^{[k]}$ was given by

$$\Gamma_i^{[k]} = \begin{cases} \gamma^{[k]} & if \left|\alpha_{c_j}^{[k]} - \alpha_i^{[k]}\right| \leq \rho^{[k]} \\ \gamma^{[k]} exp\left[-\dfrac{\left(\left|\alpha_{c_j}^{[k]} - \alpha_i^{[k]}\right| - \rho^{[k]}\right)^2}{2\rho^{[k]\,2}}\right] & if \left|\alpha_{c_j}^{[k]} - \alpha_i^{[k]}\right| > \rho^{[k]} \end{cases},$$

where the parameters $\gamma^{[k]}$ and $\rho^{[k]}$ were initialized with given values as $\gamma^{[0]} \leftarrow \gamma^*$ and $\rho^{[0]} \leftarrow \rho^*$, and then they were updated in the next step 3 (Eq. 14).

Similar to α_i, the weight vector β_j was updated by

$$\beta_j^{[k+1]} \leftarrow \beta_j^{[k]} + \sum_{i=1}^{N} \Delta\beta_j^{[k]}(c_i)$$

$$\Delta\beta_j^{[k]}(c_i) = \Lambda_j^{[k]}\left(\alpha_i^{[k]} - \beta_{c_i}^{[k]}\right),$$

where c_i represents the index of the BF whose weight vector $\beta_j^{[k]}$ was closest to $\alpha_i^{[k]}$, and $\Lambda_j^{[k]}$ was given by

$$\Lambda_j^{[k]} \equiv \begin{cases} \gamma^{[k]} & if \left|\beta_{c_i}^{[k]} - \beta_j^{[k]}\right| \leq \rho^{[k]} \\ \gamma^{[k]} exp\left[-\dfrac{\left(\left|\beta_{c_i}^{[k]} - \beta_j^{[k]}\right| - \rho^{[k]}\right)^2}{2\rho^{[k]\,2}}\right] & if \left|\beta_{c_i}^{[k]} - \beta_j^{[k]}\right| > \rho^{[k]} \end{cases}.$$

Step 3. Finally, $\gamma^{[k]}$ and $\rho^{[k]}$ were updated via

$$\gamma^{[k+1]} \leftarrow \frac{\gamma^{[k]}}{\epsilon}, \; \rho^{[k+1]} \leftarrow \epsilon\rho^{[k]}, \; 0 < \epsilon < 1. \tag{14}$$

Step 2 and Step 3 were alternatively repeated until ρ reached a given critical value of ρ_c. After completion of the cycles, if the distance between α_i and β_j was less than a certain critical value of ϵ_c, then we regarded the jth BF to be accompanying the ith BB. The algorithm described by steps 1–3 ensures a one-to-one correspondence between the BBs and BF.

In the present study, we used the following parameters: $\gamma^* = 0.01$ (pixel), $\rho^* = 10$ (pixel), $\rho_c = 0.1$ (pixel), $\epsilon = 0.99$, and $\epsilon_c = 0.1$ (pixel).

BB tracking algorithm

To construct the trajectories of individual BBs, we needed to establish a correspondence between the BBs of different frames over time. To remove the effect of stage/sample drift on BB trajectories, the BB positions at each frame were translationally moved so that those centroid would be located at the spatial origin. Let I_1 and I_1 be two successive frames containing N_1 and N_2 BBs, respectively. The tracking technique used in the present study is based on two assumptions of BB motion: (1) BBs move from one frame to the next with small displacements, and (2) BBs within a correlation length move with similar speed. The displacements were calculated using pairwise distances D_{ij} between the ith $(i = 1, ..., N_1)$ BB in one frame and the jth $(i = 1, ..., N_2)$ BB in the other. In contrast, similarity S_{ij} is evaluated by

$$S_{ij} = \frac{\sum_{m=-L/2}^{L/2}\sum_{n=-L/2}^{L/2}\left[I_1\left(m+m_{c,i},n+n_{c,i}\right) - \bar{I}_1\right]\left[I_2\left(m+m_{c,j},n+n_{c,j}\right) - \bar{I}_2\right]}{\sqrt{\sum_{m=-L/2}^{L/2}\sum_{n=-L/2}^{L/2}\left[I_1\left(m+m_{c,i},n+n_{c,i}\right) - \bar{I}_1\right]^2}\sqrt{\sum_{m=-L/2}^{L/2}\sum_{n=-L/2}^{L/2}\left[I_2\left(m+m_{c,j},n+n_{c,j}\right) - \bar{I}_2\right]^2}},$$

where m and n are pixel indices, $\left(m_{c,i(j)}, n_{c,i(j)}\right)$ represents the position of the $i(j)$th BB in the image $I_{1(2)}$, L is the correlation length, and $\bar{I}_{1(2)}$ indicates the mean intensity within an $L \times L$ window centered at $\left(m_{c,i(j)}, n_{c,i(j)}\right)$ in $I_{1(2)}$.

To establish the correspondence between BBs, we used the algorithm previously proposed by Scott and Longuet-Higgins (1991). The algorithm consists of three steps.

Step 1. The first step is to calculate a matrix named the proximity matrix M_{ij}:

$$M_{ij} = \exp\left(-\frac{D_{ij}}{2\sigma_D^2}\right) \cdot \exp\left(\frac{S_{ij}}{2\sigma_S^2}\right),$$

where σ_D is a characteristic length of BB displacements between subsequent images and σ_S represents a characteristic similarity of the motion pattern of neighboring BBs. In the present study, we set $\sigma_D = 15$ (pixel) and $\sigma_S = 0.5$.

Step 2. The next step is to find the singular value decomposition of the matrix M such that $M = U\Sigma V$, U and V are orthogonal matrices and Σ is the diagonal matrix.

Step 3. The final step is to replace all the entries of Σ by ones, resulting in the pairing matrix P: $P = UIV$, where I is the identity matrix. Each entry of P_{ij} is the measure of correspondence between the ith BB in one frame and the jth BB in the other. If an entry of P_{ij} is the maximum value of both the row i and the column j, then the ith BB is considered to correspond to the jth BB. The orthogonality of P ensures a one-to-one correspondence between the BBs in different frames.

Estimation of the amount of MTs around BBs from immunofluorescence images

Our method for estimating the amount of apical MTs has some limitations. First, MTs at the apical layer of MCCs are interspersed with hundreds of BBs. Considering that the barrel-shaped BB consists of nine triplets of MTs (Anderson, 1972; Tateishi et al., 2013), we cannot exclude the possibility that the visualized apical MTs were mixed with

artifactual signals from the BB structure. Second, the decoration of MTs with anti–tubulin antibodies hinders the visualization of individual MTs, which typically overlapped with each other in the late stage of BB alignment (Fig. 4 A in the alignment pattern). Thus, the actual distribution of overlapping MTs may be underestimated. Our method presents an approximate comparison of the MTs covering the surface of MCCs at different stages rather than the actual number of apical MTs.

Method. The algorithm to estimate the amount of MTs around BBs in a single cell has four steps: (1) extraction of the cell boundary; (2) determination of the most in-focus z-plane of BBs; (3) detection of MTs; and (4) calculation of the surface coverage of MTs.

Step 1: Extraction of the cell boundary. The boundary of a single cell at each z-slice was extracted by manually tracing the line of the Vangl1 fluorescence signal located at the cell periphery.

Step 2: Determination of the most in-focus z-plane of BBs. The most in-focus z-plane of the BBs in a single cell, symbolized as z_{BB}, was determined as the z-slice where the standard deviation of the fluorescence signal of Odf2 within a single cell reached its maximum value among all the z-slices.

Step 3: Detection of MTs. To detect MTs, each z-slice of the fluorescence image $I(x,y)$ of the MTs was processed by a filter that removes background noise and enhances fibrous structures. For this purpose, we used a Frangi filter (Frangi et al., 1998), which is processed as follows. Given image $I(x,y)$, a Hessian matrix of the image is first computed:

$$H_\sigma(x,y) = \begin{pmatrix} \dfrac{\partial^2 I_\sigma(x,y)}{\partial x^2} & \dfrac{\partial^2 I_\sigma(x,y)}{\partial x \partial y} \\ \dfrac{\partial^2 I_\sigma(x,y)}{\partial y \partial x} & \dfrac{\partial^2 I_\sigma(x,y)}{\partial y^2} \end{pmatrix},$$

where $I_\sigma(x,y) = I(x,y) * G_\sigma(x,y)$ is the convolution between $I(x,y)$ and $G_\sigma(x,y)$. $G_\sigma(x,y)$ denotes the Gaussian kernel with mean 0 and standard deviation σ, which corresponds to the width of MTs to be detected. Next, two eigenvalues $\lambda_1(x,y)$, $\lambda_2(x,y)$ of $H_\sigma(x,y)$ were computed ($|\lambda_1| > |\lambda_2|$), and the likelihood measurement $L_\sigma(x,y)$ of MTs was calculated as

$$L_\sigma(x,y) = \begin{cases} 0 & \text{if } \lambda_1 > 0 \\ exp\left(-\dfrac{R_B}{\sigma_B{}^2}\right)\left[1 - exp\left(-\dfrac{R_S}{\sigma_S{}^2}\right)\right] & \text{otherwise} \end{cases},$$

where $R_B = |\lambda_2/\lambda_1|$ and $R_S = \lambda_1^2 + \lambda_2^2$. The terms containing R_B and R_S filter out spurious signals from blob-like structures and noise. In the present study, we set $\sigma_B{}^2 = 1$, $\sigma_S{}^2 = 3$. Considering that the MTs to be detected are of different widths, σ is determined by maximizing the final likelihood of the MTs as

$$L(x,y) = \max_{\sigma_{min} \leq \sigma \leq \sigma_{max}} L_\sigma(x,y).$$

The range is set $\sigma_{min} = 1$, $\sigma_{max} = 2$ (pixel). The result of the Frangi filter $L(x,y)$ is a probability map of the pixels being MTs at each z-slice.

Step 4: Calculation of the surface coverage of MTs. As the aforementioned probability depends on the fluorescence intensity of the original image I, a simple averaging of this probability over the area within a single cell would not give a value that can be used to compare the amount of MTs in cells at different stages. Thus, we performed a further binarization of the probability map to change $L(x,y)$ into the surface coverage of MTs, which is a more robust quantity for comparing the amount of MTs. This binarization was performed at each z-slice. To ensure the reliability of our analysis, we examined a different threshold $\bar{L}$ for the binarization that was computed using n-fold of the mean of the values of $L(x,y)$ within a single cell ($n = 0.5$ to ~1.0). We verified that the results of our analysis did not qualitatively change as long as n ranged from 0.5 to 1.0. The pixels with a value larger (or smaller)

than the threshold $\bar{L}$ were treated as MTs (or background) and assigned a value of 1 (or 0). Considering that the fluorescence signal of Odf2 comes from the z-position, which is slightly higher than the BB plane (Fig. 3 A), the surface coverage of MTs around BBs was calculated by averaging the values of the binarized maps over two z-slices located at $z = z_{BB} - 2\Delta z$ and $z_{BB} - 3\Delta z$, where $\Delta z (= 150$ nm) represents the distance between neighboring z-slices. This choice of z-slices enabled us to effectively remove signals from cilia.

Measurement of the apical surface area

To measure the apical surface area of MCCs, the cell boundaries in an MTEC sheet were stained with antibodies against ZO-1. The apical surface area of a single MCC was determined as the area confined by ZO-1 and measured using IMAGEJ software (National Institutes of Health).

Notes for the mathematical model

1. Linear stability analysis. To investigate how the model described in the Materials and methods allowed for spatially inhomogeneous patterns, we performed a linear stability analysis. The model Eqs. 9 and 10 have a steady-state solution: $u^* = 0$, $c^* = \kappa_p$. To this solution, we add small perturbations of the form $\delta u = (\Delta u) exp[\omega\tau + iq \cdot r]$, $\delta c = (\Delta c) exp[\omega\tau + iq \cdot r]$, where ω is the linear growth rate, $q = (q_x, q_y)$ is the wave vector, and $\Delta u = (\Delta u_x, \Delta u_y)$ and Δc are amplitudes of the spatial perturbation. Inserting $u = u^* + \delta u$, $c = c^* + \delta c$ into Eqs. 9 and 10 and retaining the first-order terms of Δu and Δc yields the following linear equations:

$$M\begin{pmatrix} \Delta u_x \\ \Delta u_y \\ \Delta c \end{pmatrix} = \begin{pmatrix} 0 \\ 0 \\ 0 \end{pmatrix},$$

$$M \equiv \begin{pmatrix} i\kappa_p q_x & i\kappa_p q_y & \omega + q^2 + 1 \\ v_1 q^2 + v_2 q_x^2 + 1 & v_2 q_x q_y & -i\dfrac{\kappa_c}{(1+\kappa_p)^2}q_x \\ v_2 q_x q_y & v_1 q^2 + v_2 q_y^2 + 1 & -i\dfrac{\kappa_c}{(1+\kappa_p)^2}q_y \end{pmatrix},$$

where $q^2 \equiv |q|^2$. The condition of $det(M) = 0$ yields the dispersion relation:

$$\omega(q) = -1 - q^2 + \frac{\kappa_c \kappa_p q^2}{(1+\kappa_p)^2 [(v_1 + v_2)q^2 + 1]}.$$

$\omega(q)$ has a peak at the positive wave number

Table 1. The variables and parameters of the model

Symbol	Meaning	Value
$u(r,t)$	Velocity of cytoskeleton	—
$c(r,t)$	Concentration of cytoskeleton	—
$R_i(t)$	Position of the ith BB	—
v_1	Shear viscosity coefficient	0.01[a,b] and 0.09[c]
v_2	Bulk viscosity coefficient	0.03[a,b] and 0.27[c]
κ_c	Strength of contractile stress	13
κ_p	Polymerization rate	3.5,[a] 0.5,[c] and 0.1[b]
κ_r	Strength of repulsive interaction	1
κ_s	Strength of steric interaction	200
α	Amplitude of velocity fluctuation	0.05
ρ	Radius of a BB	0.5

[a]The value used in Fig. 7 C.
[b]The value used in Fig. 7 E.
[c]The value used in Fig. 7 D.

$$q = q^* \equiv \frac{1}{\sqrt{v_1 + v_2}}\left[\sqrt{\frac{\kappa_c \kappa_p}{(1+\kappa_p)^2}} - 1\right]^{\frac{1}{2}},$$

and the spatial pattern with the wavenumber q^* dominantly grows, and hence, spontaneous pattern formation occurs if the following condition is satisfied (Fig. 7 B):

$$\kappa_c > \kappa_c^* \equiv \frac{(1+\kappa_p)^2}{\kappa_p}\left(\sqrt{v_1 + v_2} + 1\right)^2.$$

2. Numerical scheme. The nondimensionalized model Eqs. 9–11 defined on a rectangular domain $L_x \times L_y$ are discretized on a square grid with spacings $h = 0.1$ by the second-order finite difference scheme. In Fig. 7 (C–E), the system size is $L_x = L_y = 150h$ and the periodic conditions are assigned to the boundary values of c and u for approximating a large system. On the other hand, to examine the boundary effects, the system size in Fig. S5 C is set as $L_x = 150h$, $L_y = 300h$ and no-slip boundary conditions are assigned to u throughout the simulation. The boundary conditions of c in Fig. S5 C remain no-flux (j = 0) during $0 \le \tau < 6$ and are changed to $j(0, y) = j(L_x, y) = 0$, $c(x, 0) = c_0$, $c(x, L_y) = 0$ during $6 \le \tau$, where c_0 is a fixed value. Note that hard walls are set at the system boundaries to confine the BBs within the system domain. For a given profile of c, Eq. 9 is solved by the Gauss–Seidel method (Press et al., 2007) to update u. Once u is known, to update c, Eq. 10 is numerically integrated with time steps $d\tau = 0.001$, using the Lax–Wendroff method (Press et al., 2007), which is accurate up to the second order in time. We repeat this set of updates until the end of the simulation. Eq. 11 is integrated by the second order Adams–Bashforth method (Press et al., 2007).

Online supplemental material

Fig. S1 shows analysis of BB alignment and verification of MTEC conditions after live imaging. Fig. S2 shows analysis of BB orientation and immunofluorescence images of apical actin and apical keratin 8 IFs in MCCs of MTECs. Fig. S3 documents the distribution of apical MTs in MCCs of MTECs revealed by super-resolution confocal microscopy and serial thin-section electron microscopy. Fig. S4 shows effects of drug treatment on BB arrays and apical cytoskeleton. Fig. S5 demonstrates spatial distribution of the cytoskeletal cross-linker plectin in MTEC multiciliated cells. Furthermore, predictive simulation of BB alignment under the regulation of a cell boundary is shown, demonstrating that asymmetric MT distribution controls the direction of BB lines. Video 1 shows beating cilia of GFP-centrin2 MTECs under normal incubation, after live imaging, and during live imaging. Video 2 shows long-term live imaging of GFP-centrin2-labeled BBs in MTEC multiciliated cells for Cell 1 and Cell 2. Video 3 shows tracking of the dynamic behavior of individual BBs in MTEC multiciliated cells. Videos 4–7 show UHVEMT images and 3D reconstruction of apical MTs in the four patterns of BB alignment. Video 8 shows live imaging of GFP-centrin2-labeled BBs in MTEC multiciliated cells under nocodazole treatment and the behavior of BBs when they lack their asymmetric structural component, the basal foot in Odf2 mutant mouse. Videos 9 and 10 show model simulations of the BB pattern in the wild-type cell, in the perturbed condition under nocodazole treatment, and in the absence of BF, respectively. Online supplemental material is available at http://www.jcb.org/cgi/content/full/jcb.201601023/DC1. Additional data are available in the JCB DataViewer at http://dx.doi.org/10.1083/jcb.201601023.dv.

References

Al Jord, A., A.-I. Lemaître, N. Delgehyr, M. Faucourt, N. Spassky, and A. Meunier. 2014. Centriole amplification by mother and daughter centrioles differs in multiciliated cells. *Nature.* 516:104–107. http://dx.doi.org/10.1038/nature13770

Anderson, R.G. 1972. The three-dimensional structure of the basal body from the rhesus monkey oviduct. *J. Cell Biol.* 54:246–265. http://dx.doi.org/10.1083/jcb.54.2.246

Antoniades, I., P. Stylianou, and P.A. Skourides. 2014. Making the connection: ciliary adhesion complexes anchor basal bodies to the actin cytoskeleton. *Dev. Cell.* 28:70–80. http://dx.doi.org/10.1016/j.devcel.2013.12.003

Banerjee, S., and M.C. Marchetti. 2011. Instabilities and oscillations in isotropic active gels. *Soft Matter.* 7:463–473. http://dx.doi.org/10.1039/C0SM00494D

Boutin, C., P. Labedan, J. Dimidschstein, F. Richard, H. Cremer, P. André, Y. Yang, M. Montcouquiol, A.M. Goffinet, and F. Tissir. 2014. A dual role for planar cell polarity genes in ciliated cells. *Proc. Natl. Acad. Sci. USA.* 111:E3129–E3138. http://dx.doi.org/10.1073/pnas.1404988111

Brooks, E.R., and J.B. Wallingford. 2014. Multiciliated cells. *Curr. Biol.* 24:R973–R982. http://dx.doi.org/10.1016/j.cub.2014.08.047

Brugués, J., and D. Needleman. 2014. Physical basis of spindle self-organization. *Proc. Natl. Acad. Sci. USA.* 111:18496–18500. http://dx.doi.org/10.1073/pnas.1409404111

Chailley, B., G. Nicolas, and M.C. Lainé. 1989. Organization of actin microfilaments in the apical border of oviduct ciliated cells. *Biol. Cell.* 67:81–90. http://dx.doi.org/10.1111/j.1768-322X.1989.tb03012.x

Chaudhuri, A., B. Bhattacharya, K. Gowrishankar, S. Mayor, and M. Rao. 2011. Spatiotemporal regulation of chemical reactions by active cytoskeletal remodeling. *Proc. Natl. Acad. Sci. USA.* 108:14825–14830. http://dx.doi.org/10.1073/pnas.1100007108

Chien, Y.-H., M.E. Werner, J. Stubbs, M.S. Joens, J. Li, S. Chien, J.A. Fitzpatrick, B.J. Mitchell, and C. Kintner. 2013. Bbof1 is required to maintain cilia orientation. *Development.* 140:3468–3477. http://dx.doi.org/10.1242/dev.096727

Elgeti, J., and G. Gompper. 2013. Emergence of metachronal waves in cilia arrays. *Proc. Natl. Acad. Sci. USA.* 110:4470–4475. http://dx.doi.org/10.1073/pnas.1218869110

Flitney, E.W., E.R. Kuczmarski, S.A. Adam, and R.D. Goldman. 2009. Insights into the mechanical properties of epithelial cells: the effects of shear stress on the assembly and remodeling of keratin intermediate filaments. *FASEB J.* 23:2110–2119. http://dx.doi.org/10.1096/fj.08-124453

Francis, R.J.B., B. Chatterjee, N.T. Loges, H. Zentgraf, H. Omran, and C.W. Lo. 2009. Initiation and maturation of cilia-generated flow in newborn and postnatal mouse airway. *Am. J. Physiol. Lung Cell. Mol. Physiol.* 296:L1067–L1075. http://dx.doi.org/10.1152/ajplung.00001.2009

Frangi, A.F., W.J. Niessen, K.L. Vincken, and M.A. Viergever. 1998. Multiscale vessel enhancement filtering. *Med. Image Anal.* 1496:130–137. http://dx.doi.org/10.1007/BFb0056195

Gordon, R.E. 1982. Three-dimensional organization of microtubules and microfilaments of the basal body apparatus of ciliated respiratory

epithelium. *Cell Motil.* 2:385–391. http://dx.doi.org/10.1002/cm.970020407

Gowrishankar, K., S. Ghosh, S. Saha, R, C, S. Mayor, and M. Rao. 2012. Active remodeling of cortical actin regulates spatiotemporal organization of cell surface molecules. *Cell.* 149:1353–1367. http://dx.doi.org/10.1016/j.cell.2012.05.008

Gromley, A., A. Jurczyk, J. Sillibourne, E. Halilovic, M. Mogensen, I. Groisman, M. Blomberg, and S. Doxsey. 2003. A novel human protein of the maternal centriole is required for the final stages of cytokinesis and entry into S phase. *J. Cell Biol.* 161:535–545. http://dx.doi.org/10.1083/jcb.200301105

Guillot, C., and T. Lecuit. 2013. Mechanics of epithelial tissue homeostasis and morphogenesis. *Science.* 340:1185–1189. http://dx.doi.org/10.1126/science.1235249

Guirao, B., and J.-F. Joanny. 2007. Spontaneous creation of macroscopic flow and metachronal waves in an array of cilia. *Biophys. J.* 92:1900–1917. http://dx.doi.org/10.1529/biophysj.106.084897

Guirao, B., A. Meunier, S. Mortaud, A. Aguilar, J.-M. Corsi, L. Strehl, Y. Hirota, A. Desoeuvre, C. Boutin, Y.-G. Han, et al. 2010. Coupling between hydrodynamic forces and planar cell polarity orients mammalian motile cilia. *Nat. Cell Biol.* 12:341–350. http://dx.doi.org/10.1038/ncb2040

Hayashi, S., and Y. Okada. 2015. Ultrafast superresolution fluorescence imaging with spinning disk confocal microscope optics. *Mol. Biol. Cell.* 26:1743–1751. http://dx.doi.org/10.1091/mbc.E14-08-1287

Higginbotham, H., S. Bielas, T. Tanaka, and J.G. Gleeson. 2004. Transgenic mouse line with green-fluorescent protein-labeled Centrin 2 allows visualization of the centrosome in living cells. *Transgenic Res.* 13:155–164. http://dx.doi.org/10.1023/B:TRAG.0000026071.41735.8e

Hirota, Y., A. Meunier, S. Huang, T. Shimozawa, O. Yamada, Y.S. Kida, M. Inoue, T. Ito, H. Kato, M. Sakaguchi, et al. 2010. Planar polarity of multiciliated ependymal cells involves the anterior migration of basal bodies regulated by non-muscle myosin II. *Development.* 137:3037–3046. http://dx.doi.org/10.1242/dev.050120

Hoh, R.A., T.R. Stowe, E. Turk, and T. Stearns. 2012. Transcriptional program of ciliated epithelial cells reveals new cilium and centrosome components and links to human disease. *PLoS One.* 7:e52166. http://dx.doi.org/10.1371/journal.pone.0052166

Ishikawa, H., R. Bischoff, and H. Holtzer. 1969. Formation of arrowhead complexes with heavy meromyosin in a variety of cell types. *J. Cell Biol.* 43:312–328.

Ishikawa, H., A. Kubo, S. Tsukita, and S. Tsukita. 2005. Odf2-deficient mother centrioles lack distal/subdistal appendages and the ability to generate primary cilia. *Nat. Cell Biol.* 7:517–524. http://dx.doi.org/10.1038/ncb1251

Jülicher, F., K. Kruse, J. Prost, and J.F. Joanny. 2007. Active behavior of the cytoskeleton. *Phys. Rep.* 449:3–28. http://dx.doi.org/10.1016/j.physrep.2007.02.018

Kitajiri, S., T. Miyamoto, A. Mineharu, N. Sonoda, K. Furuse, M. Hata, H. Sasaki, Y. Mori, T. Kubota, J. Ito, et al. 2004. Compartmentalization established by claudin-11-based tight junctions in stria vascularis is required for hearing through generation of endocochlear potential. *J. Cell Sci.* 117:5087–5096. http://dx.doi.org/10.1242/jcs.01393

Kunimoto, K., Y. Yamazaki, T. Nishida, K. Shinohara, H. Ishikawa, T. Hasegawa, T. Okanoue, H. Hamada, T. Noda, A. Tamura, et al. 2012. Coordinated ciliary beating requires Odf2-mediated polarization of basal bodies via basal feet. *Cell.* 148:189–200. http://dx.doi.org/10.1016/j.cell.2011.10.052

Labonté, G. 1999. New neural network for particle-tracking velocimetry. *Exp. Fluids.* 26:340–346. http://dx.doi.org/10.1007/s003480050297

Marchetti, M.C., J.F. Joanny, S. Ramaswamy, T.B. Liverpool, J. Prost, M. Rao, and R.A. Simha. 2013. Hydrodynamics of soft active matter. *Rev. Mod. Phys.* 85:1143–1189. http://dx.doi.org/10.1103/RevModPhys.85.1143

Matsuo, M., A. Shimada, S. Koshida, Y. Saga, and H. Takeda. 2013. The establishment of rotational polarity in the airway and ependymal cilia: analysis with a novel cilium motility mutant mouse. *Am. J. Physiol. Lung Cell. Mol. Physiol.* 304:L736–L745. http://dx.doi.org/10.1152/ajplung.00425.2012

Mayer, M., M. Depken, J.S. Bois, F. Jülicher, and S.W. Grill. 2010. Anisotropies in cortical tension reveal the physical basis of polarizing cortical flows. *Nature.* 467:617–621. http://dx.doi.org/10.1038/nature09376

Mirzadeh, Z., Y.-G. Han, M. Soriano-Navarro, J.M. García-Verdugo, and A. Alvarez-Buylla. 2010. Cilia organize ependymal planar polarity. *J. Neurosci.* 30:2600–2610. http://dx.doi.org/10.1523/JNEUROSCI.3744-09.2010

Mitchell, B., R. Jacobs, J. Li, S. Chien, and C. Kintner. 2007. A positive feedback mechanism governs the polarity and motion of motile cilia. *Nature.* 447:97–101. http://dx.doi.org/10.1038/nature05771

Mitchell, B., J.L. Stubbs, F. Huisman, P. Taborek, C. Yu, and C. Kintner. 2009. The PCP pathway instructs the planar orientation of ciliated cells in the *Xenopus* larval skin. *Curr. Biol.* 19:924–929. http://dx.doi.org/10.1016/j.cub.2009.04.018

Nakagawa, Y., Y. Yamane, T. Okanoue, S. Tsukita, and S. Tsukita. 2001. Outer dense fiber 2 is a widespread centrosome scaffold component preferentially associated with mother centrioles: its identification from isolated centrosomes. *Mol. Biol. Cell.* 12:1687–1697. http://dx.doi.org/10.1091/mbc.12.6.1687

Ohmi, K. 2008. SOM-based particle matching algorithm for 3D particle tracking velocimetry. *Appl. Math. Comput.* 205:890–898. http://dx.doi.org/10.1016/j.amc.2008.05.101

Osterman, N., and A. Vilfan. 2011. Finding the ciliary beating pattern with optimal efficiency. *Proc. Natl. Acad. Sci. USA.* 108:15727–15732. http://dx.doi.org/10.1073/pnas.1107889108

Pan, J., Y. You, T. Huang, and S.L. Brody. 2007. RhoA-mediated apical actin enrichment is required for ciliogenesis and promoted by Foxj1. *J. Cell Sci.* 120:1868–1876. http://dx.doi.org/10.1242/jcs.005306

Park, T.J., B.J. Mitchell, P.B. Abitua, C. Kintner, and J.B. Wallingford. 2008. Dishevelled controls apical docking and planar polarization of basal bodies in ciliated epithelial cells. *Nat. Genet.* 40:871–879. http://dx.doi.org/10.1038/ng.104

Press, W.H., S.A. Teukolsky, W.T. Vetterling, and B.P. Flannery. 2007. Numerical Recipes: The Art of Scientific Computing. 3rd Edition. Cambridge University Press, New York.

Prost, J., F. Jülicher, and J. Joanny. 2015. Active gel physics. *Nat. Phys.* 11:111–117. http://dx.doi.org/10.1038/nphys3224

Rauzi, M., P.-F. Lenne, and T. Lecuit. 2010. Planar polarized actomyosin contractile flows control epithelial junction remodelling. *Nature.* 468:1110–1114. http://dx.doi.org/10.1038/nature09566

Reed, W., J. Avolio, and P. Satir. 1984. The cytoskeleton of the apical border of the lateral cells of freshwater mussel gill: structural integration of microtubule and actin filament-based organelles. *J. Cell Sci.* 68:1–33.

Rodriguez-Boulan, E., and I.G. Macara. 2014. Organization and execution of the epithelial polarity programme. *Nat. Rev. Mol. Cell Biol.* 15:225–242. http://dx.doi.org/10.1038/nrm3775

Salbreux, G., J. Prost, and J.F. Joanny. 2009. Hydrodynamics of cellular cortical flows and the formation of contractile rings. *Phys. Rev. Lett.* 103:058102. http://dx.doi.org/10.1103/PhysRevLett.103.058102

Sandoz, D., B. Chailley, E. Boisvieux-Ulrich, M. Lemullois, M.C. Laine, and G. Bautista-Harris. 1988. Organization and functions of cytoskeleton in metazoan ciliated cells. *Biol. Cell.* 63:183–193. http://dx.doi.org/10.1016/0248-4900(88)90057-3

Satir, P., and E.R. Dirksen. 2011. Function-structure correlations in cilia from mammalian respiratory tract. In Comprehensive Physiology. D.M. Pollock, editor. American Physiology Association, Bethesda, MD. 473–494.

Scott, G.L., and H.C. Longuet-Higgins. 1991. An algorithm for associating the features of two images. *Proc. Biol. Sci.* 244:21–26. http://dx.doi.org/10.1098/rspb.1991.0045

Sedzinski, J., E. Hannezo, F. Tu, M. Biro, and J.B. Wallingford. 2016. Emergence of an apical epithelial cell surface in vivo. *Dev. Cell.* 36:24–35. http://dx.doi.org/10.1016/j.devcel.2015.12.013

Seifert, J.R.K., and M. Mlodzik. 2007. Frizzled/PCP signalling: a conserved mechanism regulating cell polarity and directed motility. *Nat. Rev. Genet.* 8:126–138. http://dx.doi.org/10.1038/nrg2042

Shao, D., H. Levine, and W.-J. Rappel. 2012. Coupling actin flow, adhesion, and morphology in a computational cell motility model. *Proc. Natl. Acad. Sci. USA.* 109:6851–6856. http://dx.doi.org/10.1073/pnas.1203252109

Shi, D., F. Usami, K. Komatsu, S. Oka, T. Abe, T. Uemura, and T. Fujimori. 2016. Dynamics of planar cell polarity protein Vangl2 in the mouse oviduct epithelium. *Mech. Dev.* S0925-4773(16)30035-1. In press. http://dx.doi.org/10.1016/j.mod.2016.05.002

Shimada, Y., S. Yonemura, H. Ohkura, D. Strutt, and T. Uemura. 2006. Polarized transport of Frizzled along the planar microtubule arrays in Drosophila wing epithelium. *Dev. Cell.* 10:209–222. http://dx.doi.org/10.1016/j.devcel.2005.11.016

Shimamoto, Y., Y.T. Maeda, S. Ishiwata, A.J. Libchaber, and T.M. Kapoor. 2011. Insights into the micromechanical properties of the metaphase spindle. *Cell.* 145:1062–1074. http://dx.doi.org/10.1016/j.cell.2011.05.038

Stubbs, J.L., E.K. Vladar, J.D. Axelrod, and C. Kintner. 2012. Multicilin promotes centriole assembly and ciliogenesis during multiciliate cell differentiation. *Nat. Cell Biol.* 14:140–147. http://dx.doi.org/10.1038/ncb2406

Svitkina, T.M., A.B. Verkhovsky, and G.G. Borisy. 1996. Plectin sidearms mediate interaction of intermediate filaments with microtubules and other components of the cytoskeleton. *J. Cell Biol.* 135:991–1007. http://dx.doi.org/10.1083/jcb.135.4.991

Tamura, A., and S. Tsukita. 2014. Paracellular barrier and channel functions of TJ claudins in organizing biological systems: advances in the field of barriology revealed in knockout mice. *Semin. Cell Dev. Biol.* 36:177–185. http://dx.doi.org/10.1016/j.semcdb.2014.09.019

Tateishi, K., Y. Yamazaki, T. Nishida, S. Watanabe, K. Kunimoto, H. Ishikawa, and S. Tsukita. 2013. Two appendages homologous between basal bodies and centrioles are formed using distinct Odf2 domains. *J. Cell Biol.* 203:417–425. http://dx.doi.org/10.1083/jcb.201303071

Turk, E., A.A. Wills, T. Kwon, J. Sedzinski, J.B. Wallingford, and T. Stearns. 2015. Zeta-tubulin is a member of a conserved tubulin module and is a component of the centriolar basal foot in multiciliated cells. *Curr. Biol.* 25:2177–2183. http://dx.doi.org/10.1016/j.cub.2015.06.063

Vladar, E.K., R.D. Bayly, A.M. Sangoram, M.P. Scott, and J.D. Axelrod. 2012. Microtubules enable the planar cell polarity of airway cilia. *Curr. Biol.* 22:2203–2212. http://dx.doi.org/10.1016/j.cub.2012.09.046

Werner, M.E., P. Hwang, F. Huisman, P. Taborek, C.C. Yu, and B.J. Mitchell. 2011. Actin and microtubules drive differential aspects of planar cell polarity in multiciliated cells. *J. Cell Biol.* 195:19–26. http://dx.doi.org/10.1083/jcb.201106110

Wiche, G., S. Osmanagic-Myers, and M.J. Castañón. 2015. Networking and anchoring through plectin: a key to IF functionality and mechanotransduction. *Curr. Opin. Cell Biol.* 32:21–29. http://dx.doi.org/10.1016/j.ceb.2014.10.002

You, Y., E.J. Richer, T. Huang, and S.L. Brody. 2002. Growth and differentiation of mouse tracheal epithelial cells: selection of a proliferative population. *Am. J. Physiol. Lung Cell. Mol. Physiol.* 283:L1315–L1321. http://dx.doi.org/10.1152/ajplung.00169.2002

Zhao, H., L. Zhu, Y. Zhu, J. Cao, S. Li, Q. Huang, T. Xu, X. Huang, X. Yan, and X. Zhu. 2013. The Cep63 paralogue Deup1 enables massive de novo centriole biogenesis for vertebrate multiciliogenesis. *Nat. Cell Biol.* 15:1434–1444. http://dx.doi.org/10.1038/ncb2880